

COSMOLOGICAL CONSTRAINTS FROM GALAXY CLUSTERING AND THE MASS-TO-NUMBER RATIO OF GALAXY CLUSTERS

JEREMY L. TINKER¹ ERIN S. SHELDON², RISA H. WECHSLER³, MATTHEW R. BECKER^{4,5}, EDUARDO ROZO^{4,5,9},
YING ZU⁶, DAVID H. WEINBERG⁶, IDIT ZEHAVID⁷, MICHAEL R. BLANTON¹, MICHAEL T. BUSH⁸, BENJAMIN P. KOESTER⁴

¹Center for Cosmology and Particle Physics, Department of Physics, New York University, New York, NY 10013

²Brookhaven National Laboratory, Upton, NY 11973

³Kavli Institute for Particle Astrophysics & Cosmology, Physics Department, and Stanford Linear Accelerator Center, Stanford University, Stanford, CA 94305

⁴Kavli Institute for Cosmological Physics, Chicago, IL 60637

⁵Department of Astronomy & Astrophysics, University of Chicago, Chicago IL 6037

⁶Department of Astronomy, Ohio State University, Columbus, OH 43210

⁷Department of Astronomy & CERCA, Case Western Reserve University, Cleveland, OH 44106

⁸Institute for Theoretical Physics, Department of Physics, University of Zurich, CH-8057, Switzerland

⁹Einstein Fellow

Draft version January 19, 2013

ABSTRACT

We place constraints on the average density (Ω_m) and clustering amplitude (σ_8) of matter using a combination of two measurements from the Sloan Digital Sky Survey: the galaxy two-point correlation function, $w_p(r_p)$, and the mass-to-galaxy-number ratio within galaxy clusters, M/N , analogous to cluster M/L ratios. Our $w_p(r_p)$ measurements are obtained from DR7 while the sample of clusters is the maxBCG sample, with cluster masses derived from weak gravitational lensing. We construct non-linear galaxy bias models using the Halo Occupation Distribution (HOD) to fit both $w_p(r_p)$ and M/N for different cosmological parameters. HOD models that match the same two-point clustering predict different numbers of galaxies in massive halos when Ω_m or σ_8 is varied, thereby breaking the degeneracy between cosmology and bias. We demonstrate that this technique yields constraints that are consistent and competitive with current results from cluster abundance studies, even though this technique does not use abundance information. Using $w_p(r_p)$ and M/N alone, we find $\Omega_m^{0.5} \sigma_8 = 0.465 \pm 0.026$, with individual constraints of $\Omega_m = 0.29 \pm 0.03$ and $\sigma_8 = 0.85 \pm 0.06$. Combined with current CMB data, these constraints are $\Omega_m = 0.290 \pm 0.016$ and $\sigma_8 = 0.826 \pm 0.020$. All errors are 1σ . The systematic uncertainties that the M/N technique are most sensitive to are the amplitude of the bias function of dark matter halos and the possibility of redshift evolution between the SDSS Main sample and the maxBCG cluster sample. Our derived constraints are insensitive to the current level of uncertainties in the halo mass function and in the mass-richness relation of clusters and its scatter, making the M/N technique complementary to cluster abundances as a method for constraining cosmology with future galaxy surveys.

Subject headings: cosmology: observations—galaxies:clustering—galaxies:clusters

1. INTRODUCTION

Galaxy clustering measurements offer a unique window into the distribution of dark matter in the universe. The recently completed Sloan Digital Sky Survey (SDSS; York et al. 2000, Abazajian et al. 2009) provides unprecedented precision and accuracy in its map of the local universe. However, one of the main impediments to the use of galaxy clustering for inferring cosmological information is galaxy bias—it is probable that the distribution of galaxies differs from the distribution of dark matter. Thus both the amplitude and shape of the galaxy clustering signal are biased relative to the clustering of dark matter at quasi-linear and nonlinear scales. This bias is degenerate with cosmology in such a way that a bias model can be constructed to match the observed real-space galaxy two-point correlation function for a range of cosmological models (Yang et al. 2004; Tinker et al. 2005; Yoo et al. 2006; Zheng & Weinberg 2007). In this paper, we combine real-space galaxy clustering and the cross-correlation of galaxies with galaxy clusters. The mass scale of the clusters is determined by weak gravitational lensing from Sheldon et al. (2009b), which provides the leverage to break the degeneracy and constrain cosmological parameters.

The framework within which we construct the bias model is the Halo Occupation Distribution (HOD; see,

e.g., Peacock & Smith 2000; Seljak 2000; Scoccimarro et al. 2001; Berlind & Weinberg 2002; Cooray & Sheth 2002). In this model, all galaxies are contained within dark matter halos with a probability distribution $P(N|M)$, the probability that a halo of mass M contains N galaxies of a given class. We define a dark matter halo as a collapsed, virialized object with a mean interior density of 200 times the critical density. The statistics governing the spatial distribution of dark matter can be estimated with analytic models (e.g., Press & Schechter 1974; Cole & Kaiser 1989; Mo & White 1996; Sheth & Tormen 1999; Sheth et al. 2001; Ma et al. 2010), but they are most accurately calibrated through N -body simulations (Jenkins et al. 2001; Seljak & Warren 2004; Warren et al. 2006; Reed et al. 2007; Tinker et al. 2008a; Pillepich et al. 2010; Tinker et al. 2010). These simulations specify the mass function of dark matter halos, the large-scale bias of halos, and their quasi-linear clustering relative to the clustering of the matter distribution itself. Thus, once the HOD is constructed with a model for the internal distribution of galaxies within halos, this relationship between galaxies and halos fully specifies the spatial distribution of galaxies on all scales. The key ingredient within $P(N|M)$ is the mean number of galaxies as a function of halo mass, $\langle N \rangle_M$. Distinct cosmologies produce distinct populations of dark matter halos (Zheng et al. 2002), thus for each cosmology there is a

distinct $P(N|M)$ and $\langle N \rangle_M$ such that the model matches the same galaxy two-point correlation function $\xi_g(r)$.

Data sets that are sensitive to the underlying mass scale of dark matter halos can break the bias-cosmology degeneracy (Zheng & Weinberg 2007). The most direct measurement is the mean number of galaxies in halos of mass M . In this paper we will use the ratio of these two quantities, M/N . This measurement is most easily made in the most massive halos—galaxy clusters. Cluster-sized halos are the largest collapsed structures in the dark matter density distribution, making them relatively easy to locate observationally and providing myriad methods with which to estimate their masses. The M/N measurement is analogous to the mass-to-light ratio of dark matter halos, M/L . In previous decades, M/L of galaxy clusters was utilized as a method for inferring the dark matter density parameter Ω_m (e.g., Gott et al. 1974; Peebles 1986; Bahcall et al. 1995, 2000; Carlberg et al. 1996; Rines et al. 2004). The pivotal assumption in this method was that the mean M/L of clusters was representative of the mean M/L of the universe, thus $\Omega_m = \langle M/L \rangle \times \rho_{\text{lum}} / \rho_{\text{crit}}$, where ρ_{lum} is the luminosity density and ρ_{crit} is the critical density. These results were among the first to challenge the prevailing theoretical expectation that $\Omega_m = 1$. However, efforts to use this relation yielded values of Ω_m near 0.1, in significant tension with a large array of other methods that were converging on a ‘concordance’ cosmology of $\Omega_m = 0.3$ and $\sigma_8 = 0.9$ (e.g., Spergel et al. 2003; Tegmark et al. 2004; Seljak et al. 2005). However appealing, the assumption that clusters are representative had little theoretical support (Bardeen et al. 1986), and the lack of agreement between cluster M/L and other measures of Ω_m strongly implied that they are biased objects.

In Tinker et al. (2005), we demonstrated that cluster M/L ratios depend not only on the matter density but also on the amplitude of density fluctuations, σ_8 , once the galaxy bias model is constrained to match the projected galaxy correlation function $w_p(r_p)$. Combining M/L measurements of clusters in the CNOC2 survey (Carlberg et al. 1996) with early clustering results from SDSS (Zehavi et al. 2005), we determined that these data constrain a degeneracy curve $(\Omega_m/0.3)^{0.6}(\sigma_8/0.9) = 0.75 \pm 0.06$. This degeneracy is similar to that constrained by measurements of the abundances of galaxy clusters; ‘cluster normalized’ models that lie on the same value of $\Omega_m^\gamma \sigma_8$ predict the same number of clusters, where γ is usually around 0.4–0.6 (Rozo et al. 2010). These results were in good agreement with those of van den Bosch et al. (2003), who combined clustering in the Two Degree Field Galaxy Redshift Survey (Norberg et al. 2001) with cluster M/L and first-year CMB results from WMAP (Spergel et al. 2003). Vale & Ostriker (2006) reached similar conclusions using a subhalo abundance matching method, again drawing on cluster M/L ratios. All of these studies demonstrated that the ‘concordance’ values of $(\Omega_m, \sigma_8) = (0.3, 0.9)$ could not simultaneously account for the clustering of galaxies and the M/L of clusters. These conclusions were validated when three-year WMAP results emerged in excellent agreement in the Ω_m - σ_8 plane (Spergel et al. 2007) with the M/L result of $(\Omega_m/0.3) \times (\sigma_8/0.9)^{0.6} = 0.75 \pm 0.06$ from Tinker et al. (2005). The key revision to the WMAP estimates was improved correction of polarization foregrounds, which reduced the estimated electron scattering optical depth, and which thereby reduced the matter fluctuation amplitude inferred from the CMB anisotropy amplitude.

Although the confirmation with later CMB data demonstrated the potential of this approach, both the

van den Bosch et al. (2003) and Tinker et al. (2005) studies paid little attention to the possible systematic errors in the use of halo occupation methods, emphasizing instead the systematic uncertainties in cluster M/L estimates. This paper, we use the largest data sets currently available. For the clustering we use measurements from Data Release 7 of the SDSS (Abazajian et al. 2009), which covers nearly a quarter of the sky to obtain close to a million galaxy redshifts. Our cluster sample comes from the maxBCG cluster catalog (Koester et al. 2007a), consisting of over 10^4 optically-detected clusters. These massive data sets close the door on statistics-limited analyses; in this paper we take great care to quantify the systematic uncertainties in our theoretical model. Our knowledge of the statistics of dark matter halos is not perfect, and our assumptions for how galaxies populate halos are not infallible. Thus we will incorporate these uncertainties into our analysis in order to yield robust constraints on cosmological parameters.

This paper is structured as follows: In section 2 we present our clustering data and our measurements of M/N from the maxBCG clusters. In section 3 we describe our theoretical model for both $w_p(r_p)$ and M/N within the HOD framework, demonstrating how this method is sensitive to different cosmologies. In section 4 we present a detailed description of the systematic uncertainties in our analysis. In section 5 we present our results, showing constraints in the Ω_m - σ_8 plane and constraints on HOD parameters. In section 6 we discuss these results in context with other studies that utilize clusters as a cosmological tool and present prospects for the future with the M/N method. We briefly summarize in section 7.

2. DATA

2.1. Galaxy Clustering Measurements

Our galaxy clustering measurements are obtained from 7300 deg² of sky, slightly smaller than the full SDSS DR7 of 7900 deg² (Abazajian et al. 2009). The methodology is described in detail by Zehavi et al. (2010; hereafter Z10). Briefly, we choose three volume-limited samples of galaxies on which to focus our analysis: $^{0.1}M_r < -19.5$, $^{0.1}M_r < -20.5$, and $^{0.1}M_r < -21.0$ (also listed in Table 1)¹. These samples have complementary attributes for this analysis. The $M_r < -20.5$ sample, which corresponds approximately to a sample of all galaxies brighter than L_* , is the optimal sample for this type of analysis; the magnitude limit is bright enough such that the volume contained suppresses sample variance in the clustering measurement, but it has a high enough number density that the $\langle N \rangle_M$ will be above unity for the mass range probed in the sample of clusters we use. The fainter sample, $M_r < -19.5$ maximizes the signal-to-noise in the M/N measurement, while the brighter sample, $M_r < -21.0$, has the smallest sample variance for the clustering measurement. The galaxy clustering measurements are only weakly correlated because z_{max} is different for each sample, minimizing the overlapping volume (see Table 1).

The clustering quantity we utilize for each sample is the projected two-point galaxy autocorrelation function, $w_p(r_p)$. This statistic is defined as

¹ We do not assume a value of h for galaxy magnitudes, but for brevity we write absolute magnitudes as M rather than $M - 5 \log h$. The superscript indicates the redshift to which the magnitude is k -corrected using the algorithm of Blanton & Roweis (2007).

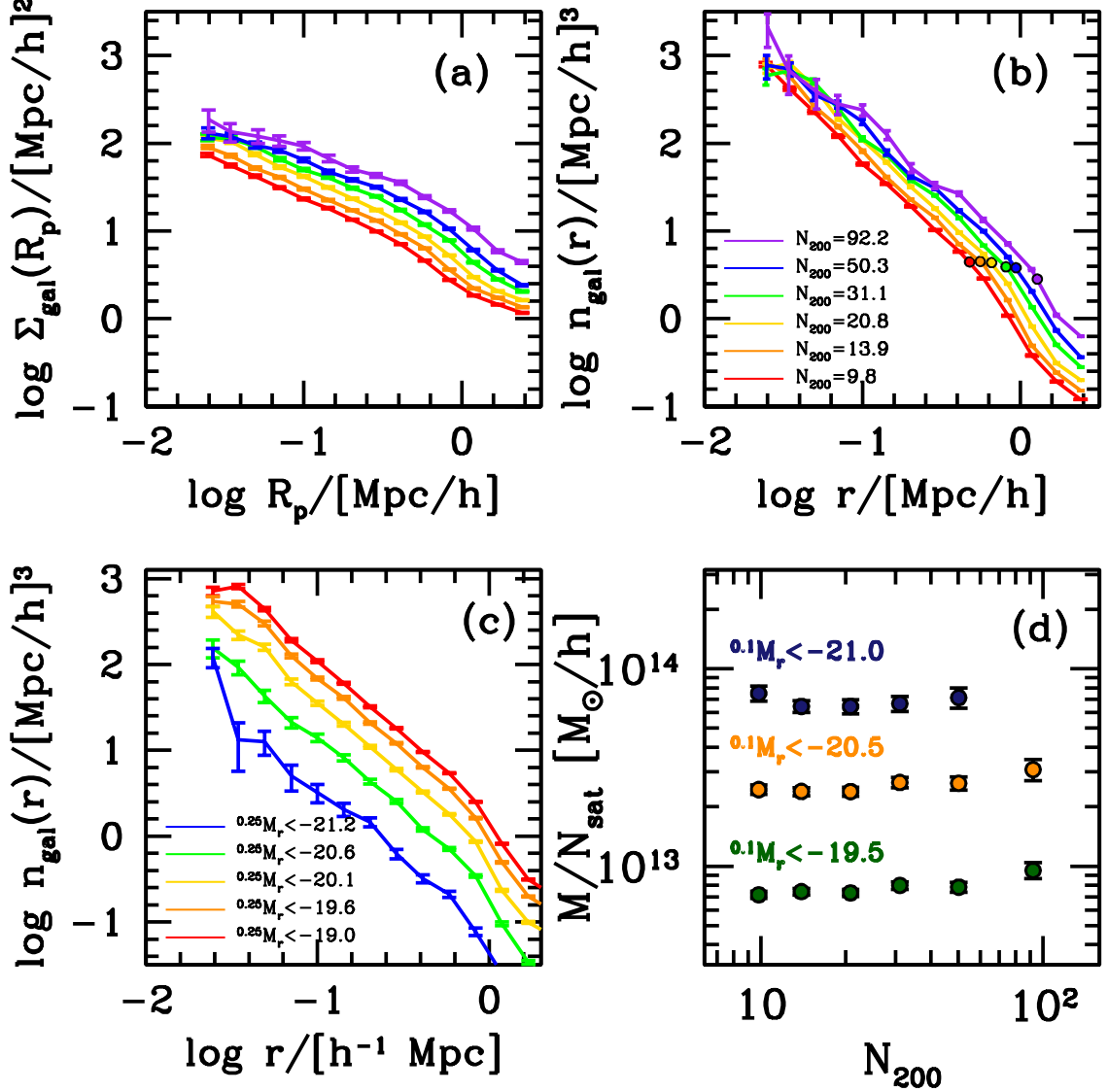


FIG. 1.— Panel (a): The background-subtracted projected galaxy number density around maxBCG clusters of varying richness (see key in panel [b]). These measurements are for galaxies brighter than $^{0.25}M_r = -19.0$. Panel (b): The deprojected number density profiles of galaxies for the data in panel (a). The filled circle indicates the halo radius R_{N200} for each richness bin. Panel (c): The variation in $n_{\text{gal}}(r)$ as a function of magnitude threshold. Panel (d): The M/N measurements as a function of cluster richness. The data are labeled by their $^{0.1}M_r$ magnitude thresholds (see Table 1 for the conversion between $^{0.1}M_r$ and $^{0.25}M_r$). Note that we define N to include on satellite galaxies. These data do not include the correction for miscentering, discussed in §4.

$$w_p(r_p) = 2 \int_0^{\pi_{\text{max}}} \xi(r_p, \pi) d\pi, \quad (1)$$

where r_p is the projected separation between two galaxies, π is the line-of-sight separation between two galaxies, and $\xi(r_p, \pi)$ is the measured two-dimensional correlation function. Due to the peculiar motions of galaxies against the Hubble flow, $\xi(r_p, \pi)$ is anisotropic. Integrating along the π direction minimizes the effects of redshift space anisotropies, allowing for an easier comparison to analytic models. If $\pi_{\text{max}} = \infty$, redshift space effects are eliminated entirely, but the finite volume of the survey requires that we limit the integral to $\pi_{\text{max}} = 40 h^{-1} \text{Mpc}$. At this π_{max} , redshift-space effects on $w_p(r_p)$ are larger than the error bars on the DR7 measurements at scales of $r_p \gtrsim 5 h^{-1} \text{Mpc}$. Although it is possible to include redshift-space anisotropies in HOD calculations

of the non-linear two-point correlation function (e.g., Tinker 2007), we limit our analysis to $r_p < 3 h^{-1} \text{Mpc}$ to eliminate any systematic biases due to redshift-space effects. Our theoretical model for $w_p(r_p)$ utilizes the Smith et al. (2003) fitting function for the nonlinear matter $\xi(r)$, thus limiting our analysis to small scales eliminates biases from possible errors in the Smith et al. (2003) prescription. Measurements at these scales provide more than enough statistical power for our constraints given the systematic uncertainties discussed in §4, which dominate our final error budget.

We use the full covariance matrix for each clustering sample. The covariance matrix is estimated through the data using the jackknife technique. The full survey is divided into 104 subsamples of roughly equal sky area (thus nearly equal volume), and each subsample is removed from the survey and $w_p(r_p)$ is re-measured. The jackknife cumulative covariance

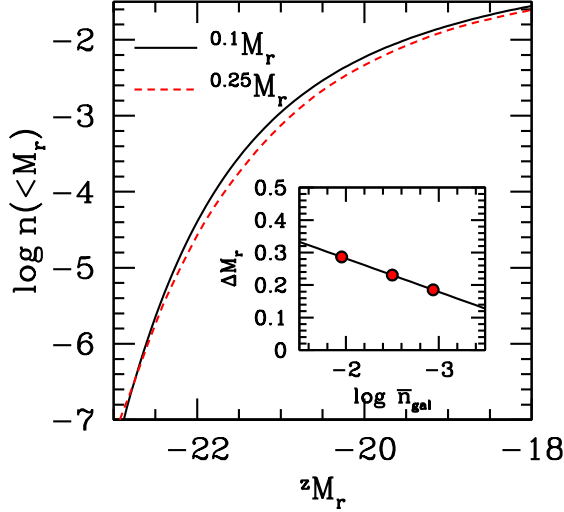


FIG. 2.— The evolution of the r -band cumulative luminosity function between $z = 0.1$ and $z = 0.25$. The black curve shows the measurements from Blanton et al. (2003). The dashed curve represents our estimate of the $0.25 M_r$ luminosity function based on the method of Blanton (2006). The inset panel shows $\Delta M_r = 0.25 M_r - 0.1 M_r$. The three filled points indicate the number densities of our three $z = 0.1$ Main galaxy samples. See Table 1 for the exact values of $0.25 M_r$ for the three $0.1 M_r$ thresholds.

estimate is

$$\sigma_{ij}^2 = \frac{N-1}{N} \sum_{l=1}^N (w_{p,i}^l - \bar{w}_p) (w_{p,j}^l - \bar{w}_p), \quad (2)$$

where subscripts i and j denote bins of r_p and superscript l denotes the subsample. The factor of $(N-1)/N$ corrects for the fact that the variance is calculated with samples that are slightly smaller than the full sample, thus the variance of the subsamples will be larger approximately by the ratio of the volumes. The accuracy of these error estimates is discussed by Z10; see also Norberg et al. (2009), who conclude that jackknife errors are generally accurate or conservative on the scales investigated here.

2.2. The maxBCG Cluster Catalog

The maxBCG algorithm (Koester et al. 2007b) utilizes the high fraction of early-type galaxies within clusters to identify massive halos as overdensities of bright, uniformly red galaxies. The large number of such galaxies within each cluster and the tightness of their color distribution allow for accurate photometric redshift estimates. Using mock galaxy catalogs, the algorithm is optimized to have completeness and purity above 90%, or higher as richness increases. The algorithm produces a richness estimate for each object, N_{200} , that is defined as the number of red-sequence galaxies brighter than $0.25 M_i = -19.2$ within an aperture containing a mean overdensity of such galaxies that is 200 times the mean density of galaxies. This aperture scales roughly with the virial radius of the halo, thus larger halos have larger apertures (Hansen et al. 2005). The richness estimate is not to be confused with the occupation number in the HOD; N in the HOD refers to *all* the galaxies (not just red) brighter than a defined magnitude threshold within the exact halo radius. The richness N_{200} , although correlated with N to some degree, is used exclusively as a reference value with which to bin clusters. Because the

magnitude limit for maxBCG selection is significantly fainter than that of even our $0.1 M_r < -19.5$ sample, and the aperture within which maxBCG counts member galaxies is not identical to the actual halo radius, the values of N are lower than those of N_{200} , by roughly a factor of two for $0.1 M_r < -19.5$ and larger factors for brighter thresholds (see Table 2 below; also recall that N_{200} includes central galaxies while N counts only satellites).

The maxBCG catalog (Koester et al. 2007a) is a sample of clusters identified in 7398 deg² of SDSS imaging data, roughly the same as the imaging samples released in DR4 (Adelman-McCarthy et al. 2006). For our analysis here, we utilize a subset of this imaging data that was analyzed in Sheldon et al. (2009b) and Sheldon et al. (2009a) consisting of 6325 deg². The redshift range of the clusters in the sample is $0.1 \leq z \leq 0.3$, yielding a nearly volume-limited sample of clusters. Although the catalog identifies clusters with $N_{200} \geq 3$, we restrict our analysis to clusters with $N_{200} \geq 9$. Objects with a richness below this value suffer from a higher degree of uncertainty due to projection effects. We bin the clusters into 6 richness bins listed in Table 2. We note that our catalog differs slightly from the publicly released catalog in Koester et al. (2007a), which was limited to clusters with $N_{200} \geq 10$.

The average masses of clusters in each richness bin are obtained from the weak gravitational lensing analysis of Sheldon et al. (2009b). All the clusters in each bin are stacked, yielding a high signal-to-noise estimate of the projected density contrast profile, $\Delta \Sigma(R_p)$. This profile is de-projected and integrated out to a radius at which the mean interior density is $\Delta = 200 \rho_{\text{crit}}$, thereby yielding an estimate of the mean cluster mass within each bin. We define this radius as R_{N200} . We differentiate this radius from R_{200c} , which is the radius for a specific halo, while R_{N200} is a quantity specific to each richness bin². The weak lensing measurements and additional tests with X-ray measurements and velocity dispersions of maxBCG clusters demonstrate that N_{200} correlates strongly with dark matter mass, but there is also a scatter between mass and richness (Becker et al. 2007; Rykoff et al. 2008; Rozo et al. 2009). This scatter and its uncertainties are characterized by Rozo et al. (2009).

The cluster masses in Sheldon et al. (2009b) are subject to a number of biases. First, this analysis assumes that brightest cluster galaxy (BCG) identified by the algorithm is located at the true bottom of the gravitational potential of the dark matter halo. Tests on mock galaxy catalogs reveal that this is not true in $\sim 10\%$ of observed objects, a fraction that increases monotonically with decreasing richness (Johnston et al. 2007). This ‘miscentering effect’ lowers the measured mass relative to the true mass. Additionally, errors in the photometric redshifts of the sample of background sources behind the clusters also affect the measured halo mass (see the discussion in Rozo et al. 2009). The uncertainties in scatter, miscentering, and weak lensing systematics are all taken into account in this study. In particular, the Sheldon et al. (2009b) weak lensing masses are estimated to be biased low by $18 \pm 6\%$ (Roza et al. 2009). We will discuss their quantitative incorporation in the analysis in §4. One advantage of our M/N analysis is that it is much less sensitive than abundance analysis to miscentering errors, since these tend to affect mass and galaxy occupation

² Note that R_{N200} is different from the quantity R_{200} , defined in Hansen et al. (2005) as the radius at which the mean interior *galaxy* density within clusters is 200 times the mean galaxy density.

in similar ways.

2.3. Measuring the Number of Galaxies in Clusters

To determine the number of satellite galaxies per halo, a stacking technique is also used. In each stacked richness bin, the total projected galaxy counts are measured in bins of $\log R_p$. To determine the number of galaxies that are associated with the cluster and not chance projection, the same process of stacking is done with a set of random pointings with the same redshift distribution as the clusters. In each bin of $\log R_p$, the mean number of galaxies from the random projections is subtracted from the mean number around the stacked clusters. Full details of this procedure are given by Sheldon et al. (2009a) and Hansen et al. (2009).

Figure 1a shows the projected galaxy number density profiles for the six richness bins in Table 2. These results are shown for galaxies brighter than $^{0.25}M_r = -19.0$. The density profiles do not include the BCG of each cluster, which is located at $R_p = 0$. Thus these data represent satellite galaxies only. The error bars are obtained through jackknife resampling in the plane of the sky with patches of 6.3 deg^2 . To obtain the number of galaxies within R_{N200} , $\Sigma_{\text{gal}}(R_p)$ is inverted to recover the three-dimensional density profile. The inversion is performed using the standard Abel-type integral,

$$n_{\text{gal}}(r) = \frac{1}{\pi} \int_r^\infty dR_p \frac{-\Sigma_{\text{gal}}(R_p)}{\sqrt{r^2 - R_p^2}}. \quad (3)$$

The projected density is not measured out to infinity, thus in practice we fit a power law to the three highest- R_p data points and truncate the integral at $30 h^{-1} \text{ Mpc}$. Making this upper limit twice as large results in negligible differences in the density profiles obtained within the cluster radii. Figure 1b shows the inverted three-dimensional density profiles of the satellite galaxies. The filled circles indicate the cluster radius in each richness bin. These density profiles are integrated out to R_{N200} to determine the total halo occupation of satellite galaxies in each richness bin. Figure 1c shows how the number density profiles depend on luminosity threshold for a fixed richness bin, $\langle N_{200} \rangle = 20.8$ in this example. As expected, the number of galaxies increases monotonically with decreasing luminosity threshold at all scales.

The clustering measurements described in §2.1 are for the Main sample of SDSS galaxies, which probe $z \sim 0.1$. The median redshift of the maxBCG catalog is $z \sim 0.25$. For proper analysis, we require a consistent sample of galaxies between both redshifts. Because the luminosity function evolves between these two redshifts, and because $^{0.25}M_r$ is not equivalent to $^{0.1}M_r$, we choose to define $z = 0.25$ samples that have the same number density as the Main samples. Figure 2 compares the $^{0.1}M_r$ luminosity function (Blanton et al. 2003) to our estimate of the $^{0.25}M_r$ luminosity function using the technique of Blanton (2006) and employed in the Sheldon et al. (2009a) analysis. The Blanton (2006) technique uses measurements of the luminosity function at $z \sim 0.1$ and $z \sim 1$ to constrain the amount of luminosity evolution and number density evolution in both the red sequence and the blue cloud across this redshift baseline. These results are used constrain simple star formation histories of blue and red galaxies that are used to interpolate the total galaxy luminosity function at $z = 0.25$. The inset panel shows the magnitude shifts between $^{0.1}M_r$ and $^{0.25}M_r$ at the three $z = 0.1$ magnitude thresholds. We will discuss the systematic uncertainties of this approach in §4.

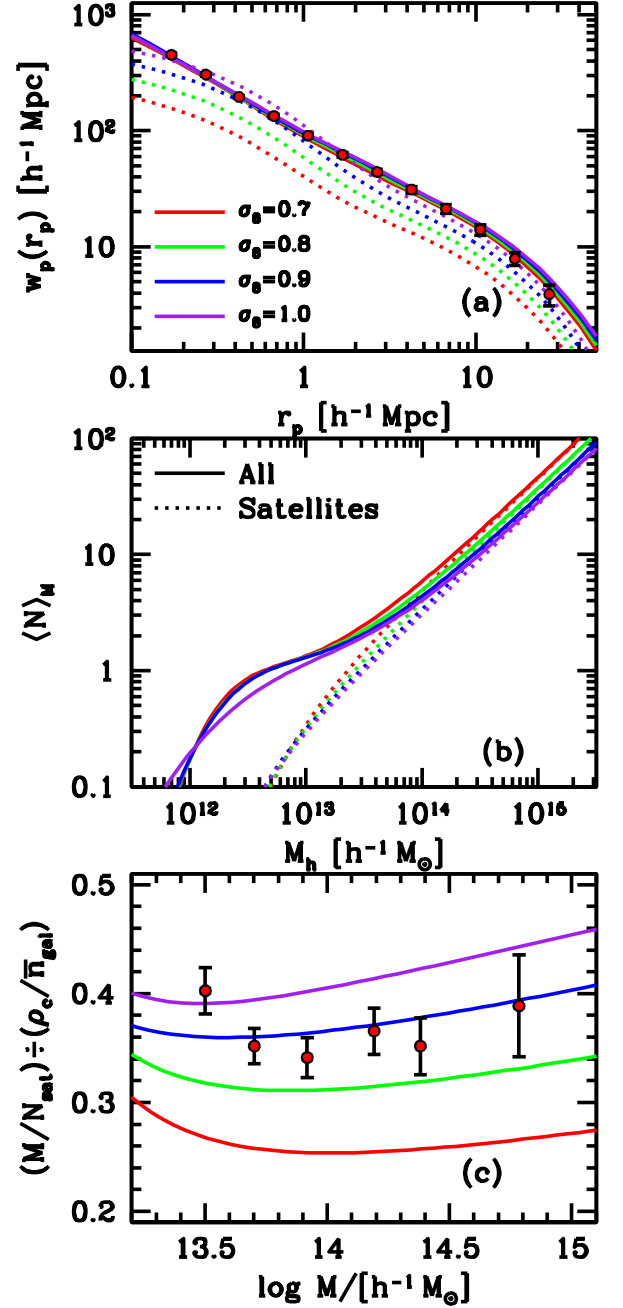


FIG. 3.— A pedagogical demonstration of the M/N method. Panel (a): The circles show the projected correlation function, $w_p(r_p)$, measured for $^{0.1}M_r < -20.5$ galaxies in DR7. The solid curves show HOD model fits to these data; in each model, the value of σ_8 is changed. The dotted lines correspond to the projected correlation function for the dark matter in each cosmological model. Panel (b): The occupation functions inferred from the best-fit models to $w_p(r_p)$ for each value of σ_8 . As σ_8 decreases, the amplitude of $\langle N \rangle_M$ at high masses increases. Panel (c): The points with errors show the maxBCG measurements for M/N (now with the miscentering correction from Figure 4 applied). The curves show the predictions for this quantity for each value of σ_8 . For convenience, we have plotted M/N as a function of halo mass rather than cluster richness, though in actual model fitting we use richness.

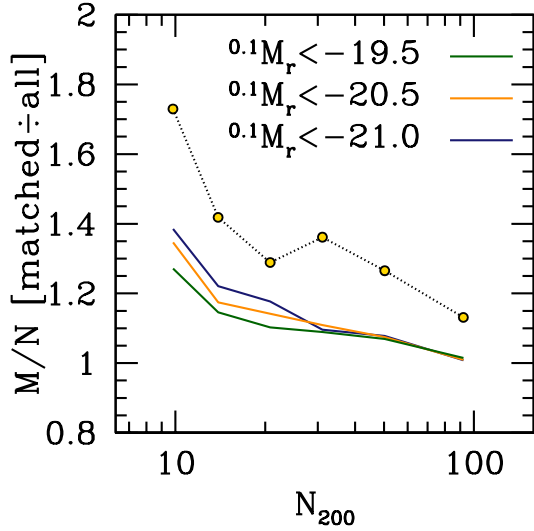


FIG. 4.— The effect of cluster miscentering on M/N in mock galaxy catalogs. The solid curves show the ratio of M/N measured from a sample of clusters that are well-matched to halos in the mock catalog to M/N measured on the full sample of clusters determined in the mock. Miscentering lowers both the mass and the number of galaxies within clusters, but the effect largely cancels in the ratio. The dotted curve connecting the open circles indicates the effect of miscentering on the halo masses derived from the $\Delta\Sigma(R_p)$ measurements in Johnston et al. (2007). In the mock, both M and N are measured from the projected mass and number density, respectively, around the clusters detected in the mock. We use the mean of all three curves as the miscentering correction on the data, and use the maximal difference of the three curves as the error in that correction.

The error bars on $n_{\text{gal}}(r)$ are correlated, thus to be conservative we assume that the errors are 100% correlated; we determine the errors on $N_{\text{sat}}(< M_r^{\text{lim}})$ by increasing or decreasing every $n_{\text{gal}}(r)$ datum by its 1σ error and re-integrating. Our $n_{\text{gal}}(r)$ data are measured on a grid of threshold $^{0.25}M_r$ values spaced by 0.28 magnitudes. For each threshold, we integrate $n_{\text{gal}}(r)$ out to R_{N200} to obtain N_{sat} and interpolate to obtain N_{sat} for the exact values of $^{0.25}M_r$ that yields the same number density as the $^{0.1}M_r$ samples (cf. Figure 2). The values and uncertainties of $N_{\text{sat}}(< M_r^{\text{lim}})$ for our three magnitude threshold values are listed in Table 2. Figure 1d shows the resulting M/N ratio for our three $^{0.1}M_r$ magnitude thresholds. Note that the N in M/N here and throughout this work refers to the number of satellite galaxies, a choice that makes M/N approximately constant from bin to bin, which would not be the case if we included central galaxies. To determine the statistical error on M/N , we sum in quadrature the fractional errors on N_{sat} and M from the weak lensing measurements in Sheldon et al. (2009b). We have 17 total M/N data points, 6 for the $^{0.1}M_r < -19.5$ and $^{0.1}M_r < -20.5$ samples, and 5 for the $^{0.1}M_r < -21.0$ sample. For the brightest sample, the richest bin does not have enough clusters to obtain a robust density profile. Values of our M and N measurements for the maxBCG sample are listed in Table 3.

When comparing M/N measurements to model predictions, we must account for the fact that the M in the M/N ratio is the same value for all three magnitude threshold samples. Thus the errors are correlated between the samples. We define a covariance matrix for the 17 M/N data points where $i = 1 - 6$ represent the $^{0.1}M_r < -19.5$ sample, $i = 7 - 12$ represents $^{0.1}M_r < -20.5$, and $i = 13 - 17$ represents $^{0.1}M_r < -21$. Most of the off diagonal elements of the covariance matrix are

zero, but, for example, data points 1, 7, and 13 are correlated because the halo mass is the same for these three data points. The diagonal elements of the covariance matrix are obtained by total differential error on the M and N data,

$$C_{ii} = \sigma_{M_i}^2 \left(\frac{\partial(M/N)_i}{\partial M_i} \right)^2 + \sigma_{N_i}^2 \left(\frac{\partial(M/N)_i}{\partial N_i} \right)^2. \quad (4)$$

The off-diagonal terms are also calculated in the same manner. For example, $C_{1,7}$ is a non-zero element expressed by

$$C_{1,7} = \sigma_M^2 \frac{\partial(M/N)_1}{\partial M} \frac{\partial(M/N)_7}{\partial M}, \quad (5)$$

where M for the two M/N data points is the same value. We note that accounting for this covariance makes little difference in our results; the uncertainties in the M/N measurements are dominated by systematics that we will discuss in §4.

As can be seen in Figure 1d, the M/N ratio is roughly independent of cluster richness. In most models of halo occupation, the number of satellite galaxies scales as a power-law with host halo mass. Most results from observed galaxy clustering, as well as N-body simulations, yield a power-law index close to unity, which would imply $M/N \sim \text{constant}$ (Kravtsov et al. 2004; Zheng et al. 2005; Conroy et al. 2006; van den Bosch et al. 2007; Tinker et al. 2007; Zheng et al. 2007; Yang et al. 2008).

3. THEORETICAL MODELING

3.1. Galaxy Two-Point Correlation Function

We parameterize the halo occupation function as two separate functions, one representing the occupation of central galaxies and one for the occupation of satellite galaxies. For central galaxies, we use the standard expression

$$\langle N_{\text{cen}} \rangle_M = \frac{1}{2} \left[1 + \text{erf} \left(\frac{\log M - \log M_{\text{min}}}{\sigma_{\log M}} \right) \right], \quad (6)$$

where M_{min} formally represents the mass at which a halo has a 50% probability of containing a central galaxy bright enough to be contained within the sample. The parameter $\sigma_{\log M}$ is related to the scatter in halo mass at fixed luminosity. Functionally, this parameter controls how “sharp” the transition is between halos that host no galaxies and halos that have one central galaxy. Because halo mass is monotonically related to clustering strength over most of the halo mass spectrum, the value of $\sigma_{\log M}$ correlates with the large-scale bias of the model; a higher scatter brings more low-mass halos into the sample, and due to the steepness of the halo mass function the resulting large-scale bias is reduced. When $M \lesssim M_*$, bias is relatively independent of halo mass³, thus $\sigma_{\log M}$ has little effect on $w_p(r_p)$. For this reason, we allow $\sigma_{\log M}$ to be a free parameter for the $^{0.1}M_r < -20.5$ and $^{0.1}M_r < -21$ samples, but we fix it at $\sigma_{\log M} = 0.2$ for the faint $^{0.1}M_r < -19.5$ sample. In our modeling we adopt a flat prior of $0.05 < \sigma_{\log M} < 1.6$. Values of $\sigma_{\log M} < 0.05$ are indistinguishable from $\sigma_{\log M} = 0$, while values of $\sigma_{\log M} > 1.6$ would be unphysical.

For satellite galaxies, we adopt an occupation function of the form

$$\langle N_{\text{sat}} \rangle_M = \langle N_{\text{cen}} \rangle_M \times \left(\frac{M}{M_{\text{sat}}} \right)^{\alpha_{\text{sat}}} \exp \left(\frac{-M_{\text{cut}}}{M} \right). \quad (7)$$

³ We define the non-linear mass scale M_* as the mass at which the linear matter variance on the Lagrangian scale of the halo is $\sigma(M) = 1.686$.

TABLE 1
SDSS DR7 SPECTROSCOPIC CLUSTERING SAMPLES

$^{0.1}M_r$	$^{0.25}M_r$	z_{med}	z_{max}	N_{gal}	$\bar{n}_g/(h^{-1} \text{ Mpc})^{-3}$
-19.5	-19.21	0.068	0.083	112497	1.11×10^{-2}
-20.5	-20.27	0.104	0.131	117588	3.16×10^{-3}
-21.0	-20.81	0.126	0.160	77381	1.15×10^{-3}

NOTE. — The number density is corrected for incompleteness. $^{0.25}M_r$ is the magnitude threshold at $z = 0.25$ with the same number density as the corresponding $^{0.1}M_r$.

TABLE 2
MAXBCG CLUSTER SAMPLE

N_{200} range	$M_{N200}/10^{13} h^{-1} \text{ M}_{\odot}$	$N(^{0.1}M_r < -19.5)$	$N(^{0.1}M_r < -20.5)$	$N(^{0.1}M_r < -21)$	miscentering	$R_{N200} h^{-1} \text{ Mpc}$
9-11	3.17 ± 0.12	4.06 ± 0.08	1.25 ± 0.04	0.450 ± 0.029	1.33 ± 0.06	0.59
12-17	5.04 ± 0.16	6.21 ± 0.11	2.00 ± 0.06	0.772 ± 0.042	1.18 ± 0.04	0.70
18-25	8.28 ± 0.30	10.40 ± 0.22	3.31 ± 0.13	1.258 ± 0.082	1.14 ± 0.04	0.82
26-40	15.54 ± 0.59	17.81 ± 0.41	5.57 ± 0.23	2.26 ± 0.16	1.098 ± 0.009	1.01
41-70	24.0 ± 1.1	27.92 ± 0.85	8.78 ± 0.48	3.40 ± 0.31	1.074 ± 0.004	1.17
71-220	60.9 ± 4.5	58.0 ± 3.1	18.8 ± 1.7	—	1.011 ± 0.003	1.60

NOTE. — Note: The halo masses are equivalent to those in Sheldon et al. (2009a) with an 18% correction factor as discussed in Rozo et al. (2009). The N values refer only to satellite galaxies and are given for the equivalent $^{0.1}M_r$ thresholds; see text for details. The values listed are the raw measurements that do not include the correction for miscentering. The ‘miscentering’ column indicates the factor, and its error, by which all N measurements are multiplied to correct for miscentering.

Equation (7) parameterizes satellite occupation as a power-law at high halo masses with an exponential cutoff at low masses, motivated by the results of high-resolution N-body and hydrodynamic simulations of galaxy formation (Kravtsov et al. 2004; Zheng et al. 2005; Conroy et al. 2006; Wetzel & White 2010). The factor of $\langle N_{\text{cen}} \rangle_M$ in equation (7) ensures $\langle N_{\text{sat}} \rangle_M \leq \langle N_{\text{cen}} \rangle_M$ at all masses.

We assume that satellite galaxies follow a spatial distribution within the dark matter halo of an NFW density profile (Navarro et al. 1997). However, we do *not* assume that the galaxies trace the dark matter within the halos. The concentration parameter of NFW profile, c_{gal} , is a multiple of the concentration parameter of the dark matter, $f_{\text{con}} \equiv c_{\text{gal}}/c_m$. The proportionality constant f_{con} is left as a parameter in our analysis with a flat prior of $[0.2, 2.0]$, which brackets the extreme scenarios for the spatial bias between satellite galaxies and dark matter within halos. Thus the *shape* of the concentration-mass relation is the same as the dark matter, but the normalization is allowed to vary. For the dark matter, we use the concentration-mass relation of Bullock et al. (2001) with the parameters of Wechsler et al. (2006).

To calculate the mean number of pairs within each halo, we assume that the satellite galaxies are Poisson distributed about the mean. This is well supported by both numerical results (Kravtsov et al. 2004; Zheng et al. 2005; Gao et al. 2011) and observational data (Lin et al. 2004). Small deviations from Poisson like those shown in the recent results from Busha et al. (2010) and Boylan-Kolchin et al. (2010) do not have a significant effect on the clustering in this paper because they occur at subhalo masses not probed for the galaxy samples analyzed here.

We use the theoretical model of Tinker et al. (2005) to calculate the two-point correlation function in real space, with one modification. Because the mass function and bias relation used in this analysis are taken from numerical results based on

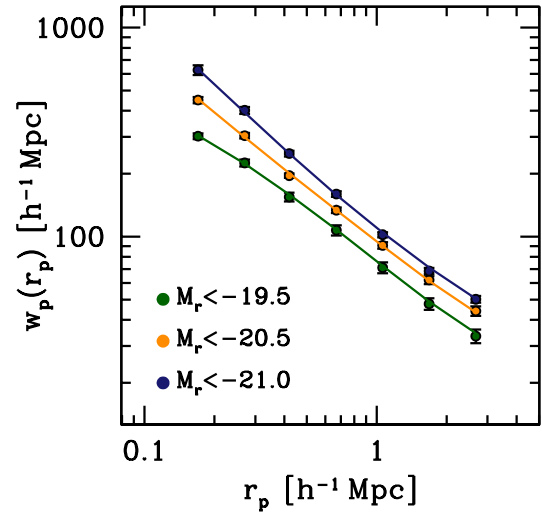


FIG. 5.— The best-fit HOD model fits to $w_p(r_p)$ for each $^{0.1}M_r$ threshold. Uncertainties in the model fits are shown in Figure 6.

spherical-overdensity (SO) halo catalogs (Tinker et al. 2008a, 2010), the halo exclusion must be modified to match this halo definition. In the SO halo finding algorithm of Tinker et al. (2008a), halos are allowed to overlap so long as the center of one halo is not contained within the radius of another halo. Thus, the minimum separation of two halos with radii $R_1 \geq R_2$ is R_1 , rather than the sum of the two radii, as done in Tinker et al. (2005).

3.2. Calculating M/N from the HOD

Measuring the galaxy content within a cluster sample stacked on richness is not identical to measuring the mean number of galaxies within the virial radii of halos of mass M . First, due to scatter in the mass-richness relation, a stack of clusters with the same N_{200} contains a sample of halos of varying mass. Second, each richness bin stacks clusters from a range of richness values (e.g., the most massive richness bin stacks all clusters with $71 \leq N_{200} \leq 220$). The halo radius for each richness bin, $R_{N_{200}}$, is determined such that the mean overdensity of all the halos in the bin is $200\rho_{\text{crit}}$. The true radii of individual halos in the bin, R_M are not identical due to scatter; some halos will be smaller the $R_{N_{200}}$ while some will be larger. Both the scatter and the fixed aperture are accounted for when we calculate M/N within our HOD models.

For each bin of N_{200} values, the expected value of M/N for a given model is computed by

$$M/N = \frac{\sum_{N_{200}} \int dM n_h(M) P(N_{200}|M) M f_h(R_{N_{200}}|M)}{\sum_{N_{200}} \int dM n_h(M) P(N_{200}|M) \langle N_{\text{sat}} \rangle_M f_{\text{gal}}(R_{N_{200}}|M)}, \quad (8)$$

where $n_h(M)$ is the halo mass function given by Tinker et al. (2008a)⁴, $P(N_{200}|M)$ is the probability of a cluster with mass M having richness N_{200} (Rozo et al. 2009), and f is the aperture correction factor for both the mass and the number of galaxies, given the fact that the radius of a halo of mass M , R_M , may be different from the fixed aperture $R_{N_{200}}$ for that richness bin. The integrals in the numerator and denominator are evaluated at each value of N_{200} in the richness bin and summed together. Note however, that $R_{N_{200}}$ is the same value within a richness bin; see the values listed in Table 2. The scatter in richness at fixed halo mass is assumed to be a log-normal of the form

$$P(N_{200}|M) dN_{200} = \frac{1}{\sqrt{2\pi}\sigma_R} \exp\left[-\frac{(\ln N_{200} - \mu_R)^2}{2\sigma_R^2}\right] \frac{dN_{200}}{N_{200}}. \quad (9)$$

The mean of this distribution is

$$\mu_R = B_R + A_R \ln(M/M_{\text{pivot}}), \quad (10)$$

where $M_{\text{pivot}} = 2.06 \times 10^{13} \times 0.7 h^{-1} M_{\odot}$, and the factor of 0.7 is to change the value listed in Rozo et al. (2009) from units of M_{\odot} to $h^{-1} M_{\odot}$. We will discuss the values and errors on the mass-richness scatter in the following section.

The aperture correction factor is small but non-negligible. For a halo with mass M , corresponding to radius R_M , and concentration $c(M)$, the mass enclosed at any radius R is calculated by

$$f_h(R|M) = \frac{1}{M} 4\pi\rho_s R^3 y^3 [\ln(1+1/y) - (1+y)^{-1}] \quad (11)$$

(c.f., appendix A in Hu & Kravtsov 2003), where $y \equiv r_s/R$ and $r_s \equiv R_M/c(M)$. Equation (11) assumes an NFW form for the halo density profile. The parameter ρ_s is a normalization parameter such that $f_h(R_M|M) = 1$. Because we assume that satellite galaxies also follow an NFW profile, we can use

⁴ The Tinker et al. (2008a) mass function is universal at a given redshift for constant values of Δ_m , the overdensity relative to the mean density in the universe. The maxBCG observations of mass and N_{gal} are made at 200 times the critical density (Δ_c) assuming a value of $\Omega_m = 0.27$ and $z = 0.25$, which translates to $\Delta_m = 508$.

the same scaling relation to determine the number of satellite galaxies within an aperture R for a halo of mass M .

$$f_{\text{gal}}(R|M) = \frac{1}{\langle N_{\text{sat}} \rangle_M} 4\pi\rho_s R_{N_{200}}^3 y^3 [\ln(1+1/y) - (1+y)^{-1}] \quad (12)$$

where ρ_s is once again determined by requiring $f_{\text{gal}}(R_M|M) = 1$. As discussed above, the concentrations parameter for satellite galaxies is defined separately from the dark matter.

3.3. Probing Cosmology with $w_p(r_p)$ and M/N

To demonstrate the power of combining $w_p(r_p)$ and M/N , Figure 3 shows both statistics for a series of cosmological models. In all panels, the four curves represent four HOD models applied to the DR7 clustering measurements of the $^{0.1}M_r < -20.5$ sample, each with different values of σ_8 . For demonstration purposes, all other cosmological parameters are fixed, and we fix $\alpha_{\text{sat}} = 1$. For each cosmological model, a good fit to the data can be found, demonstrating that cosmology and bias are degenerate for this single statistic. However, as the halo population changes with σ_8 , the halo occupation must also change in a compensatory fashion in order to obtain the same two-point clustering. In Figure 3c, M/N is shown for each of the best-fit HOD models. The low-amplitude cosmology ($\sigma_8 = 0.7$) requires a larger weighting of high-mass (and thus highly-biased) halos in order to match the observed amplitude of the galaxy clustering. This drives M/N lower relative to the other cosmologies. The theoretical predictions also depend on the value of Ω_m ; if the matter density increases, then the mass of each halo increases proportionately, but the number of galaxies per halo remains fixed. Thus Ω_m and σ_8 will be degenerate in this analysis much as they are in cluster abundance constraints

The comparison here is not one-to-one, given that the data are convolved with the mass-richness scatter and that we have not marginalized over the many free parameters in our model. Nonetheless, this plot demonstrates that the degeneracy of cosmology and bias with respect to the two-point correlation function can be broken by empirical measurements of the HOD in the form of M/N .

4. SYSTEMATIC ERRORS

Here we detail the many systematic errors that we consider in our analysis. Some are associated with theoretical uncertainties, others with observational uncertainties.

Uncertainty in the halo mass function: We use the simulation-calibrated halo mass function of Tinker et al. (2008a) in all theoretical calculations. This mass function is calibrated on spherical overdensity halos, where halo mass is defined by the mass within a spherical aperture, the same manner as the cluster mass in the maxBCG weak-lensing mass estimates. The Tinker et al. mass function also takes into account redshift evolution of the mass function, which is 10-20% between $z = 0$ and $z = 0.25$. Most of the simulations analyzed in Tinker et al. (2008a) are realizations of a single, flat- Λ CDM cosmology representative of first-year WMAP results (Spergel et al. 2003). For this cosmology, the errors on the mass function are less than 1% up to nearly $10^{15} h^{-1} M_{\odot}$. For variants around this cosmology, the simulations produce a 5% scatter. We therefore incorporate a 5% Gaussian uncertainty on the amplitude of the halo mass function, introducing a marginalization parameter $\epsilon_n = 1.0 \pm 0.05$, which represents the amplitude of the halo mass function relative to the

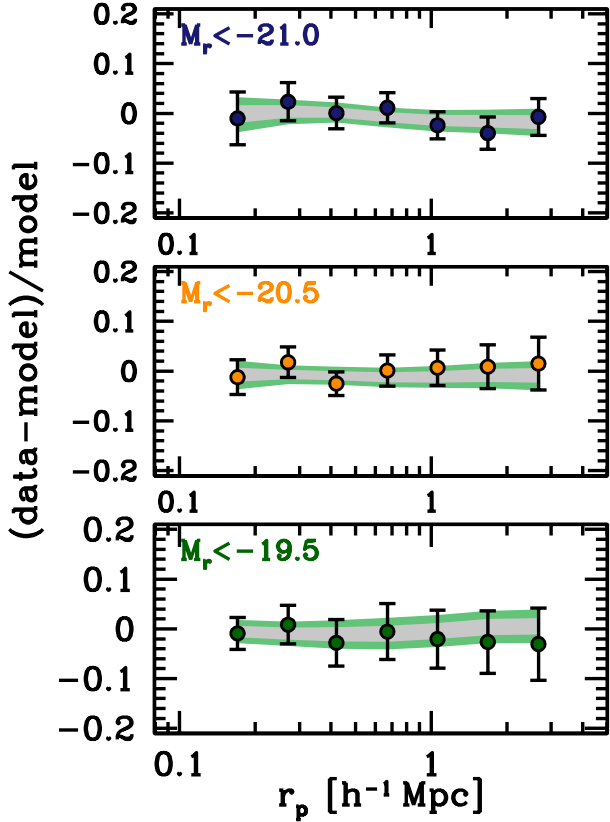


FIG. 6.— Each panel shows the fraction difference between the measurements of $w_p(r_p)$ and the best-fit model for each $^{0.1}M_r$ threshold. The contours indicate the range of models from the MCMC chain. The inner contours include 68% of all elements in the chain, while the outer contours bracket 95% of the elements in the chain. The data points are highly correlated, thus we caution the reader against χ -by-eye. Note that all models are simultaneously fit to M/N as well as $w_p(r_p)$.

Tinker et al. (2008a) fit. We describe the incorporation of this and subsequent uncertainties at the end of this section.

Uncertainty in the large-scale halo bias relation: The Tinker et al. mass function is coupled to the bias functions of Tinker et al. (2010). These bias functions are calibrated on the same N-body simulations as the mass function and with the same halo definitions. Thus, the abundance and clustering of halos are always calculated using a self-consistent halo definition. Tinker et al. (2010) find a 6% scatter in bias among the simulations. To be conservative, we implement a 6% Gaussian error on the amplitude of the halo bias relation. As with the mass function, we delineate the prior on the bias amplitude as ϵ_b , with a mean of 1.0 and an uncertainty of 0.06.

Uncertainty in the scale-dependence of the halo bias: At scales of $r \lesssim 5 h^{-1} \text{Mpc}$, halo clustering deviates from a scale-independent factor of the matter clustering. This scale dependence is minimized when the non-linear matter clustering (rather than the linear) is used to define the halo bias. We assume that the shape of the scale-dependence follows that of Tinker et al. (2005) but allow the magnitude to differ. We include a 15% Gaussian error in the deviation from constant bias, i.e.,

$$\delta b = b(r) - b_0, \quad (13)$$

where $b(r)$ is the scale-dependent bias of Tinker et al. (2005) (with a modification for very small scale halo clustering

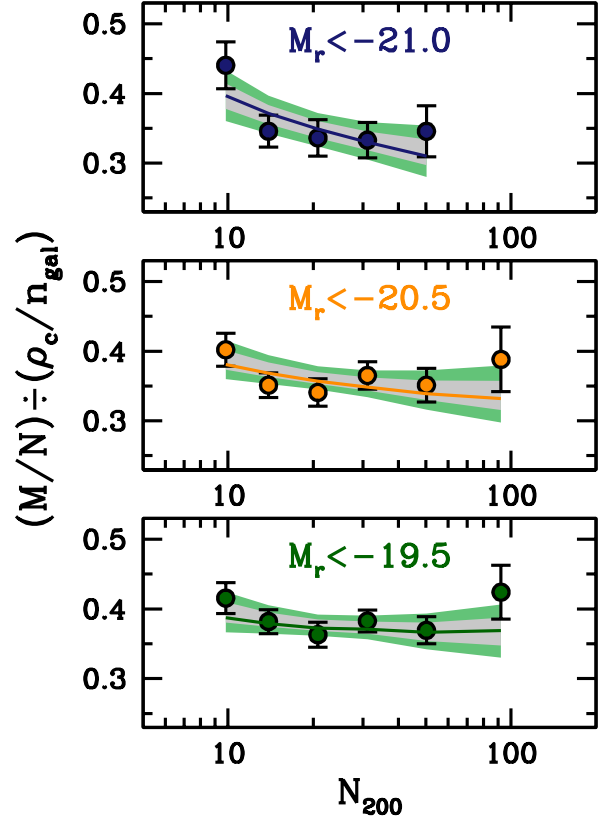


FIG. 7.— Each panel shows the M/N measurements, normalized by $\rho_{\text{crit}}/\bar{n}_g$, for each threshold sample. The solid curve in each panel shows the best-fit HOD+cosmological model. The inner and outer shaded regions bracket the 68% and 95% ranges of models in the MCMC chain, respectively. Note that all models are simultaneously fit to $w_p(r_p)$ as well as M/N .

given in Appendix A) and b_0 is the large-scale bias of Tinker et al. (2010). The Tinker et al. (2005) scale-dependent bias, $b(r)/b_0$, asymptotes to unity at $r \gtrsim 5 h^{-1} \text{Mpc}$. Parameterizing the uncertainty in the scale dependence through eq. (13) ensures that bias becomes linear at large scales. We refer to this prior as ϵ_r , with an uncertainty of 0.15.

Uncertainty in the parameters of the mass-observable relation: As described above, Rozo et al. (2009) describe the relation between halo mass and observed cluster richness from the maxBCG algorithm as a power law with parameters α_R and β_R . The scatter of mass at fixed richness is modeled as a log-normal with variance σ_R . Using X-ray data from the ROSAT All-Sky Survey, Rozo et al. (2010) both calibrate this relation and determine the uncertainties in each parameter. These are found to be

$$\begin{aligned} A_R &= 0.750 \pm 0.024 \\ B_R &= -1.09 \pm 0.09 \\ \sigma_R &= 0.35 \pm 0.07. \end{aligned}$$

These three parameters are also added to the chain with the uncertainties listed above.

Uncertainty in the evolution of the HOD: Due to the redshift baseline of our two galaxy samples, $z = 0.1$ and $z = 0.25$, we must account for possible evolution in the HOD over this narrow range. Analysis by Zheng et al. (2007) over a much larger baseline, from $z = 0.1$ to $z = 1$ using the clustering of DEEP2 galaxies, demonstrates that the $M_{\text{sat}}/M_{\text{min}}$ ratio evolves from

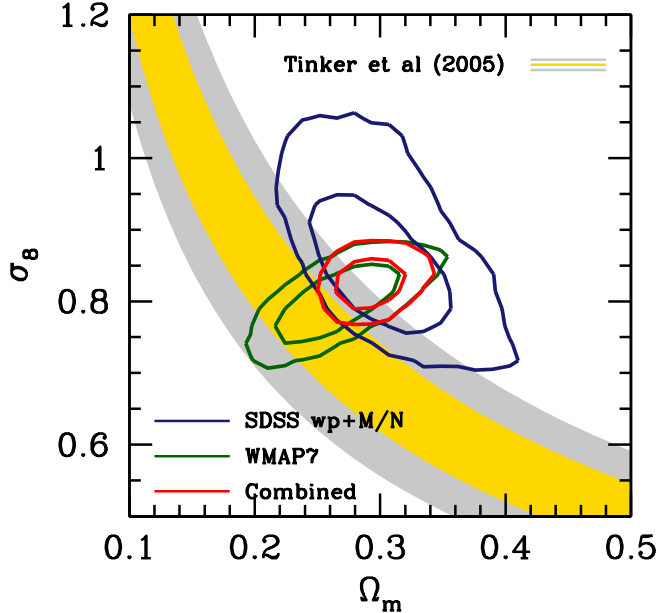


FIG. 8.— Constraints in the Ω_m - σ_8 plane, marginalizing over all other parameters and applying the priors listed in Table 3. The blue contours show 68% and 95% constraints from the M/N results. The yellow and grey shaded region indicates the 1σ and 2σ constraints, respectively, from Tinker et al. (2005). The green contour shows the constraints from WMAP7 (CMB alone, assuming a flat- Λ CDM model; Komatsu et al. 2010). The red contours show the combined constraints from M/N and WMAP7.

18 to 16 (independent of luminosity). Abbas et al. (2010) see even less evolution from $z = 0.4$ to $z = 1.1$, but using the smaller zCOSMOS data set.

We have investigated this issue theoretically in two ways: through analysis of the *Millennium* semi-analytic galaxy catalogs of Bower et al. (2006), and through the high-resolution N-body simulation Bolshoi (Klypin et al. 2010). Recall that we are analyzing samples constructed to have the same space densities at their respective redshifts, not the same magnitudes. This minimizes the effect of the evolution of the galaxy population. In the semi-analytic *Millennium* model, the HOD at fixed \bar{n}_g shows a moderate increase of 5-10% in $\langle N_{\text{sat}} \rangle_M$ at a given M from $z = 0.1$ to $z = 0.25$.

In the Bolshoi simulation, we investigate the evolution of the halo occupation of *subhalos*. The connection between substructure and galaxies is well-established (see, e.g., Kravtsov et al. 2004; Conroy et al. 2006; Moster et al. 2010; Behroozi et al. 2010 for some examples), thus this method can be used to construct galaxy catalogs without attempting to model galaxy formation physics. At fixed space density⁵, the halo occupation of subhalos shows $\lesssim 10\%$ evolution over our redshift range (Reddick et al, in preparation), varying slightly with galaxy number density. Simha et al. (2010) find that subhalo occupation statistics track the statistics of galaxy occupations in smoothed particle hydrodynamics (SPH) simulations fairly accurately, with the largest deviations arising because a small but not negligible fraction of SPH galaxies suffer dramatic stellar mass loss after entering high mass halos, thus ending up less massive than predicted.

⁵ Here we mean density of all halos and subhalos above a given maximum circular velocity. For subhalos, the value of V_{max} at the time of accretion is used to connect to galaxy luminosity.

Based on these results, we incorporate HOD evolution uncertainty as a 10% Gaussian multiplicative error on M/N , centered on no evolution.

Uncertainty in the luminosity function at $z = 0.25$: As odd as it may seem, there is no reliable measurement of the $^{0.25}M_r$ luminosity function. As discussed above and shown in Figure 2, we infer this function by the method of Blanton (2006). Although the redshift difference between the Main sample and the maxBCG sample is relatively small, the amplitude of M/N is sensitive to the details of our luminosity function estimate. The key quantities are the $^{0.25}M_r$ magnitudes that yield the same number densities as the $z = 0.1$ samples. A 0.1 mag error in these values yields a $\sim 20\%$ error in M/N . Given that the overall evolution of the luminosity function is 0.2 to 0.3 magnitudes, we use 0.1 magnitudes as a conservative error estimate on our estimate of the $z = 0.25$ luminosity function. As with the evolution of the HOD, evolution in the luminosity function shifts the amplitude of M/N , thus we include an additional 20% Gaussian multiplicative error on our theoretical calculation of M/N for a given model. The quantitative incorporation of this uncertainty with HOD evolution will be discussed at the end of this section.

Uncertainty in the calibration of the weak lensing masses: Rozo et al. (2009) apply a correction factor of 1.18 ± 0.06 to the maxBCG halo masses inferred through weak lensing in Sheldon et al. (2009b) and Johnston et al. (2007). This factor is to compensate for the fraction of sources with redshift errors large enough to place their true redshift in front of the lensing clusters, thereby diluting the shear signal. An error in halo mass scale is partly compensated by an increase in the radius at which the mean interior density is $200\rho_{\text{crit}}$, which is the radius at which N_{sat} is measured. When measuring M/N for both the original Sheldon et al. (2009b) masses and the new corrected masses, we find that the 18% increase in the mass at each richness bin yields only a 9% increase in the M/N ratio at each richness bin. The remaining 6% uncertainty in the halo masses therefore yields a 3% uncertainty in M/N . This error is correlated over all data points, and it is included with the other data systematics listed above: evolution of the HOD and the luminosity function.

Miscentering of the maxBCG algorithm: As with all optical cluster finders, maxBCG is not 100% pure and complete. Some fraction of the time, the correct halo is identified but the wrong galaxy is identified as the BCG. Additionally, chance projection of two clusters can result in the two objects being merged in the resulting cluster catalog. In the mass estimates of Sheldon et al. (2009b), these effects are not accounted for. They are also not accounted for in the measurements of the galaxy counts. Because satellite galaxies follow roughly the same distribution as the dark matter within the cluster, the effect on their ratio is significantly smaller than on either quantity individually. Rozo et al. (2010) find that the fraction of chance projections is small compared to the intrinsic scatter in the mass-richness relation, thus they conclude that the effect of projections on their constraints is negligible.

We quantify the effect of miscentering using mock galaxy catalogs on which the maxBCG algorithm is run. The mock catalogs use the ADDGALS (Adding Density Determined Galaxies to Lightcone Simulations) algorithm to populate a dark matter simulation with galaxies (Wechsler 2004; Wechsler et al preparation). Galaxies are assigned to dark matter particles based on their dark matter densities, constrained to match the observed two-point galaxy clustering statistics and

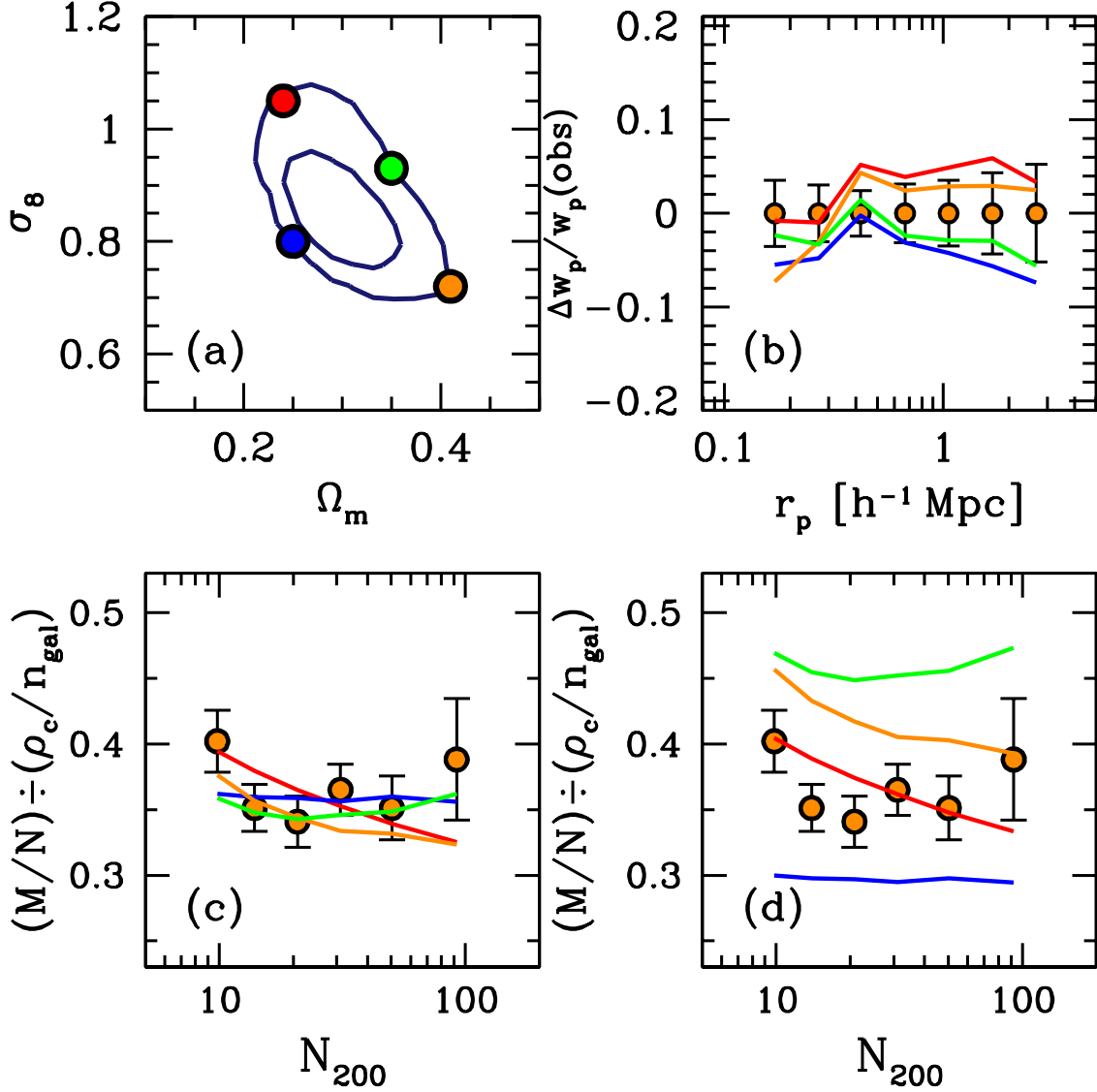


FIG. 9.— Panel (a): The circles indicate the location of four models in the Ω_m - σ_8 plane chosen from the MCMC chain. Each model is the best fitting model for that region of cosmological parameter space. Panel (b): Comparison of each model to the $w_p(r_p)$ data. The y-axis is $(w_p^{HOD} - w_p^{obs}) / w_p^{obs}$. The points with error bars are the $^{0.1}M_r < -19.5$ measurements. Panel (c): Comparison of each model to the M/N measurements, again for the $^{0.1}M_r < -20.5$ sample. The fits appear good because f_{sys} is allowed to vary from model-to-model; each model requires an unlikely value of f_{sys} to fit the data. Panel (d): The predictions of those same models when $f_{sys} = 1.13$, the value in the minimum χ^2 fit.

luminosity function, and are assigned galaxy colors based on the observed distribution of galaxy color at a given galaxy density and luminosity. Mocks created with this algorithm has been used to test the maxBCG algorithm in several previous works (e.g. Koester et al. 2007a; Johnston et al. 2007; Rozo et al. 2010; Gerdes et al. 2010). Clusters in which the detected BCG is the same as a central galaxy in a mock dark matter halo are deemed “well-matched”. Clusters where this match could not be made represent objects where the detected BCG is not a central galaxy. For the well-matched sample we repeat all the steps described in Figure 1: For each bin in richness, the mock background-subtracted surface density of galaxies is measured and inverted to obtain $n_{gal}(r)$. This quantity is integrated out to R_{halo} , yielding N_{sat} . The same process is performed on the dark matter particles as well to mimic the effect of miscentering on the weak lensing masses and the

M/N ratio. To obtain M_{halo} and R_{halo} the dark matter density profile is integrated out until $\Delta = 200\rho_{crit}$. The results are shown in Figure 4 for all three luminosity thresholds. At high richness, miscentering has a negligible effect on M/N . At $N_{200} \lesssim 20$, M/N for the well-matched sample is larger than that of the full sample of clusters. This implies that the effect of miscentering on mass is somewhat stronger than on galaxy number. However, the effect of miscentering on M/N is significantly smaller than on M by itself, as shown by the circles connected by the dotted line. Although there appears to be a monotonic effect with luminosity at low richness, it is not clear if this trend is real or noise. We take the mean of these three curves as the miscentering correction, with the range between the curves as a 1σ Gaussian error on the correction. This error is added in quadrature to the statistical errors on M/N . It is listed in Table 2.

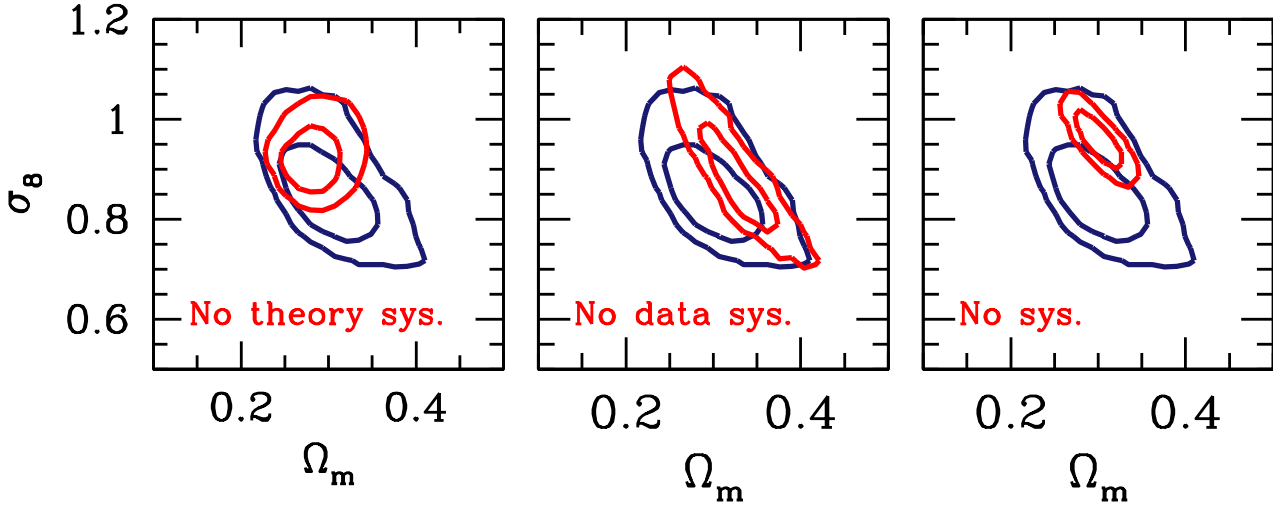


FIG. 10.— The effect of systematic uncertainties on our cosmological parameter constraints. In all panels, the blue contour show our fiducial results from Figure 8. *Left panel:* The red contour indicates the parameter constraints when reducing the uncertainty in the dark matter halo statistics by a factor of 5. Specifically, we reduce the priors on ϵ_n , ϵ_b , and ϵ_n to 0.01, 0.01, and 0.03, respectively. The dominant uncertainty in this panel is from the large-scale halo bias. *Middle Panel:* The effect of systematic uncertainties in our measurements. The red contour shows the parameter constraints when reducing the prior on f_{sys} from 0.227 to 0.02. Note that f_{sys} represents a combined effect of (in decreasing order of importance) uncertainties in the $z = 0.25$ luminosity function, evolution of the HOD from $z = 0.1$ to $z = 0.25$, and the overall calibration of weak lensing masses. *Right panel:* The red contour shows the effect of reducing *both* the theoretical and measurements uncertainties from the left two panels.

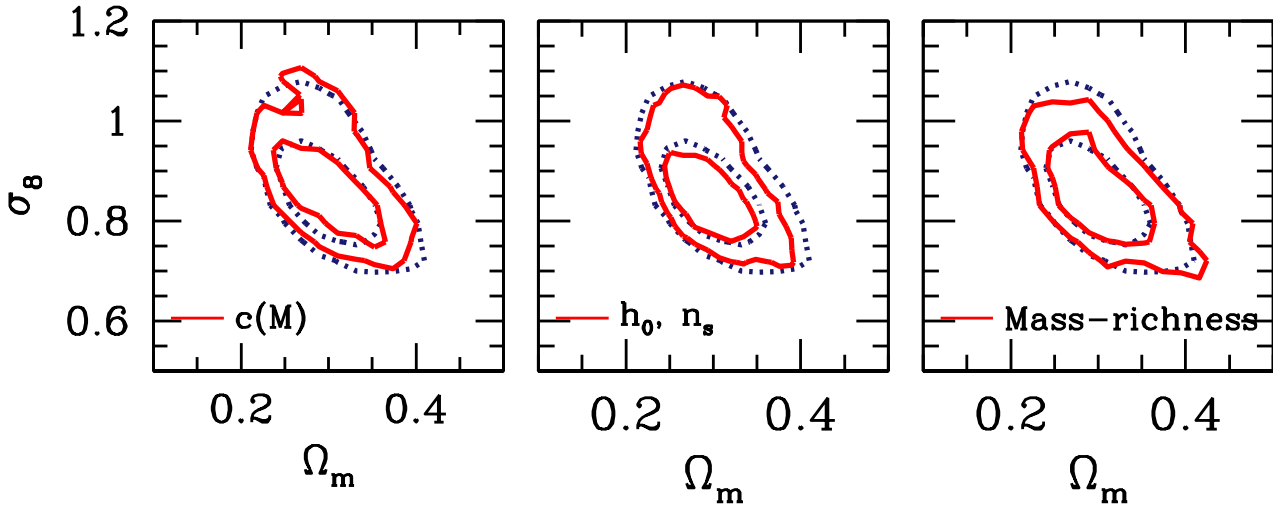


FIG. 11.— The effect of our priors on cosmological constraints. In each panel, the dotted contour shows the fiducial results from Figure 8. *Left Panel:* Red solid contours show parameter constraints when changing the prior on f_{con} from flat to a 10% Gaussian prior. *Middle Panel:* Red solid contours show parameter constraints when tightening our priors on h_0 and n_s from 0.05 and 0.03 to 0.02 and 0.01. The minimal change in the constraints shows that our results are insensitive to the allowed range in the shape of the matter power spectrum. *Right Panel:* Red solid contours show the parameter constraints obtained when tightening the priors on the mass-richness relation: B_R , A_R , and σ_R . Our fiducial errors on these quantities are 0.09, 0.024, and 0.07, respectively. The solid curves show results for uncertainties of 0.01, 0.005, and 0.01. These results indicate that the M/N method is largely insensitive to scatter in the mass-richness relation.

Environmental dependence of the HOD: It has been demonstrated that the properties of halos at fixed mass depend on large-scale environment, an effect dubbed ‘assembly bias’ (see, e.g., Gao & White 2006; Wechsler et al. 2006). Semi-analytic models of galaxy formation have predicted that this assembly bias could propagate into the properties of galaxies within halos at fixed mass (Croton et al. 2007; Zhu et al.

2006), although results from hydrodynamic simulations do not support this (Berlind et al. 2003; Yoo et al. 2006). In the standard HOD, $\langle N \rangle_M$ depends only on M and not on a second parameter, such as δ . If occupation depends on environment, then the large-scale bias of a galaxy sample may differ from that calculated through the standard HOD, biasing the results of the modeling. By modeling both $w_p(r_p)$ and the distribu-

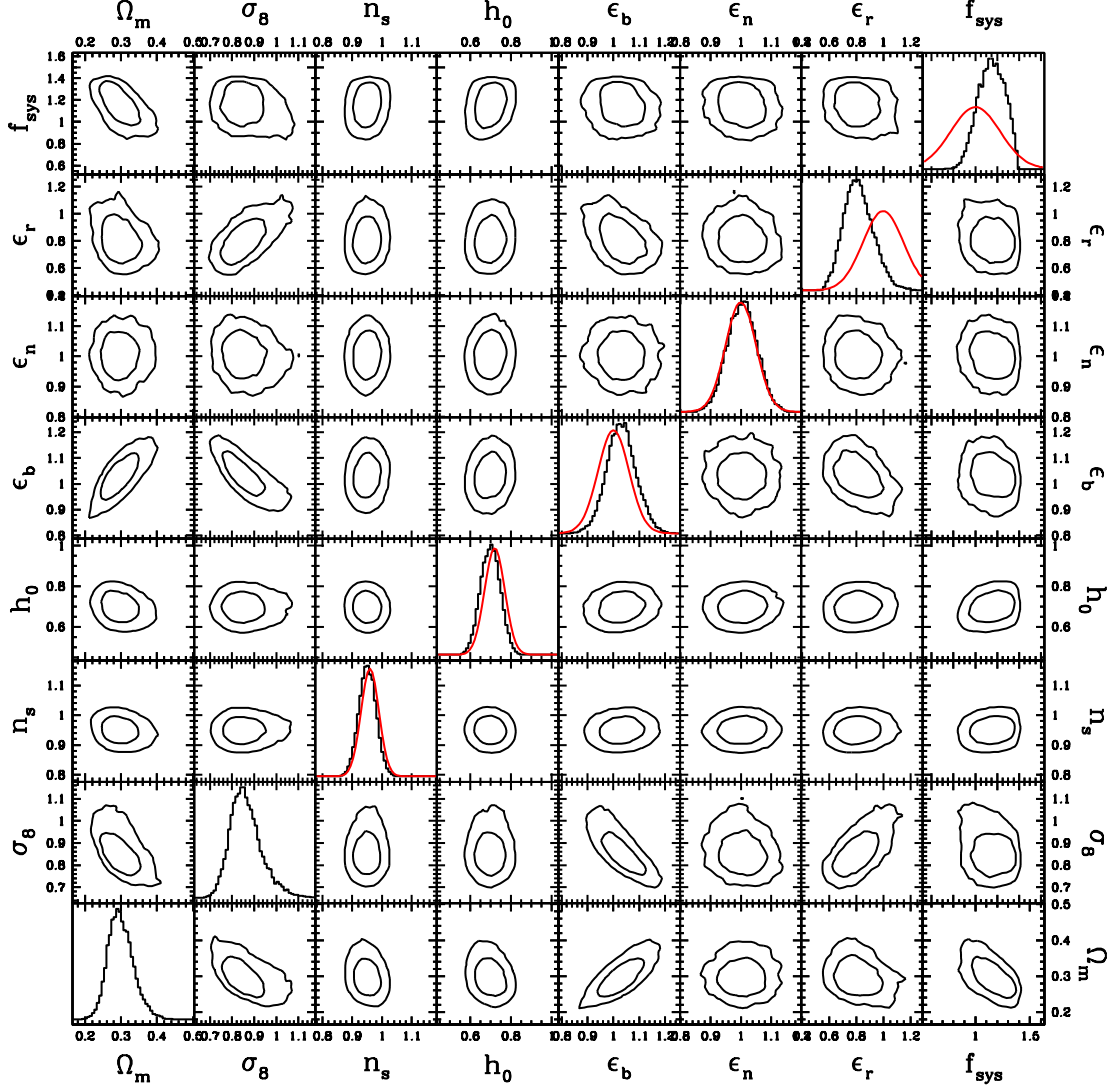


FIG. 12.— Each panel shows 68% and 95% constraints for our cosmological parameters and the marginalization parameters that encompass our systematic uncertainties. The histograms in diagonal panels shows the distribution of each parameter from the MCMC chain. The red curves in the diagonal panels show the priors on each parameter. Parameter definitions are given in Table 3.

tion of galaxy voids in the SDSS, Tinker et al. (2008b) found that any assembly bias must have less than 5% effect on the large-scale clustering of luminosity-defined samples for the luminosity range probed by SDSS data. Furthermore, our exclusion of clustering data at $r_p > 3 h^{-1} \text{Mpc}$ attenuates any impact assembly bias may have on our HOD fits. We conclude, given the small effect of assembly bias and the exclusion of large-scale data, that our 10% prior on the evolution of the HOD subsumes any error accrued due to assembly bias.

Combination: The uncertainties in evolution of the HOD, the $z = 0.25$ luminosity function, and the calibration of the weak lensing masses all have the effect of systematically shifting the M/N measurements up or down proportionately for all richness bins. These three systematic errors are uncorrelated, thus we include a $\sqrt{10^2 + 20^2 + 3^2} = 22.6\%$ systematic error on all the M/N data. To incorporate this uncertainty in the MCMC analysis, we add a ‘systematic bias parameter’ f_{sys} to the chain. For each element in the chain, the HOD pre-

diction for M/N is multiplied by f_{sys} . We enforce a Gaussian prior of 1.0 ± 0.226 on f_{sys} .

5. RESULTS

5.1. Fitting the Data

We determine constraints on all free parameters through the Monte Carlo Markov Chain (MCMC) method. For each element in the chain, we determine the χ^2 for the model in the following manner. First, χ^2 is calculated independently for all three sets of $w_p(r_p)$ measurements using the full covariance matrix for each sample. Next, the χ^2 for the 17 M/N data points is calculated using eq. (8) and the covariance matrix. The total χ^2 for each model is the sum of the two. To marginalize over the systematic uncertainty in the mass function, the parameter ϵ_n is a free parameter within the chain. For each element i in the chain, the mass function for that model is $n_{h,i}(M) = n_h(M) \times \epsilon_n$. While running the chain, we adopt a 5% Gaussian prior on this parameter. We marginalize over all

TABLE 3
LIST OF PARAMETERS

Name	Type	Value	Meaning
$^{0.1}M_r$	observational	—	SDSS r -band absolute magnitude $k+e$ corrected to $z = 0.1$.
$^{0.25}M_r$	observational	—	SDSS r -band absolute magnitude $k+e$ corrected to $z = 0.25$.
Ω_m	cosmological	no prior	matter density relative to the critical density
σ_8	cosmological	no prior	amplitude of linear matter fluctuations on the $8 h^{-1}$ Mpc scale
h_0	cosmological	0.72 ± 0.05	Hubble constant in units of 100 km/s/Mpc
n_s	cosmological	0.96 ± 0.03	spectral index of primordial fluctuations
M_{\min}	HOD	no prior	central occupation function; see eq. (6).
$\sigma_{\log M}$	HOD	[0.05, 1.6]	halo mass-galaxy luminosity scatter; see eq. (6).
M_{sat}	HOD	no prior	amplitude of the satellite occupation function; see eq. (7).
M_{cut}	HOD	no prior	cutoff of the satellite occupation function; see eq. (7).
α_{sat}	HOD	no prior	power-law slope of the satellite occupation function; see eq. (7).
f_{con}	HOD	[0.2, 2]	satellite galaxy density profile: $f_{\text{con}} \equiv c_{\text{gal}}/c_{\text{halo}}$
ϵ_n	systematic	1.00 ± 0.05	uncertainty in amplitude of halo mass function
ϵ_b	systematic	1.00 ± 0.06	uncertainty in amplitude of halo bias relation
ϵ_r	systematic	1.00 ± 0.15	uncertainty in amplitude of scale-dependent bias
f_{sys}	systematic	1.00 ± 0.22	uncertainty in the measured amplitude of M/N
B_R	maxBCG	-1.09 ± 0.09	amplitude of mass-richness relation; see eq. (10)
A_R	maxBCG	0.750 ± 0.024	slope of mass-richness relation; see eq. (10)
σ_R	maxBCG	0.35 ± 0.07	scatter in mass-richness relation; see eq. (9)
N_{200}	maxBCG (observed)	—	richness of maxBCG clusters
R_{N200}	maxBCG (observed)	—	cluster radius at which $\Delta = 200\rho_{\text{crit}}$ in a given richness bin
N_{sat}	maxBCG (observed)	—	true number of satellite galaxies in maxBCG clusters

NOTE. — The HOD parameters, M_{\min} , M_{sat} , α_{sat} , M_{cut} , f_{con} , are constrained separately for all three clustering samples. Thus there are three values of each parameter that included in the analysis. The HOD parameters $\sigma_{\log M}$ is free for the brighter two samples and fixed at $\sigma_{\log M} = 0.2$ for the faint sample. M_{\min} for each sample is set by the number density of each sample once the other HOD parameters are specified. Thus there are 14 free HOD parameters total in this analysis.

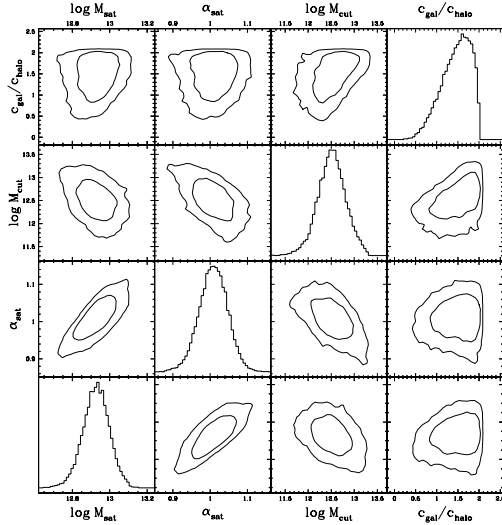


FIG. 13.— HOD parameter constraints for the $^{0.1}M_r < -19.5$ sample. The diagonal panels show the distribution of values from the MCMC chain. Note that $\sigma_{\log M}$ is not a free parameter in this sample.

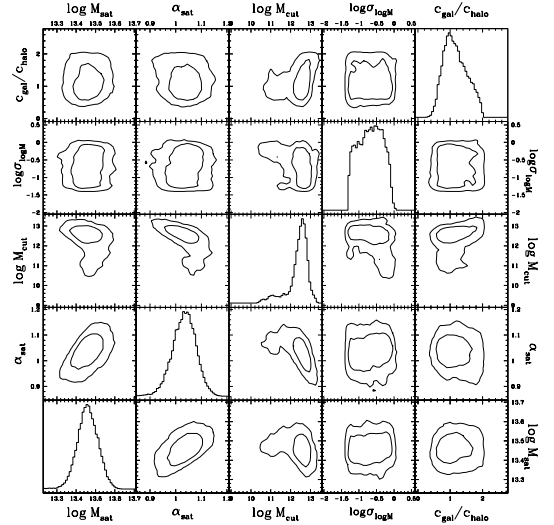


FIG. 14.— HOD parameter constraints for the $^{0.1}M_r < -20.5$ sample. The diagonal panels show the distribution of values from the MCMC chain.

other sources of systematic uncertainty in the same manner, i.e., we repeat this procedure for $\epsilon_b, \epsilon_r, f_{\text{sys}}$, and the parameters of the mass-richness relation.

Our model has a total of 21 parameters and priors. A list can be found in Table 3. There are 14 HOD parameters; each galaxy sample is modeled with an HOD of 4 or 5 parameters (we exclude $\sigma_{\log M}$ from the $^{0.1}M_r < -19.5$ sample). There are two free cosmological parameters, Ω_m and σ_8 . There are two additional cosmological priors, h_0 and n_s , which enter into the calculation of the linear matter power spectrum for

a given cosmological model, for which we use the transfer function of Eisenstein & Hu (1999). We enforce Gaussian priors on these parameters that are somewhat broader than their current uncertainties considering the latest CMB results (Komatsu et al. 2010). As we will demonstrate, the influence of these parameters is minimal, but we include them for the purpose of marginalizing over acceptable shapes of the matter power spectrum. There are 7 additional priors on our systematic errors; 3 for dark matter halo statistics, 3 for the cluster mass-richness relation, and one— f_{sys} —to incorporate sys-

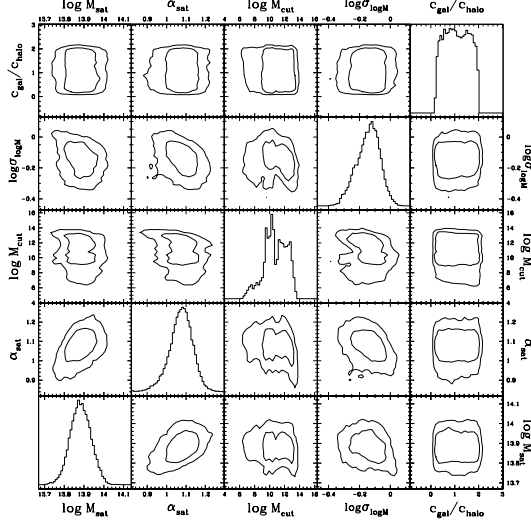


FIG. 15.— HOD parameter constraints for the $^{0.1}M_r < -21.0$ sample. The diagonal panels show the distribution of values from the MCMC chain.

tematic uncertainties in our measurements.

The χ^2 for the best-fit model is 26.9. With 16 free parameters for 38 data points, this model yields a χ^2 per degree of freedom of 1.22. The probability of drawing a value ≥ 26.9 from a χ^2 distribution with 22 degrees of freedom is 0.215. Figure 5 shows the projected correlation function measured from DR7 and the best-fit model. Due to the vanishingly small error bars, we also show the fractional differences between the model and data in Figure 6. The shaded bands show the 68% and 95% ranges in the models from the chain at each value of r_p . Figure 7 presents the maxBCG M/N measurements and the results from the MCMC chains. In each panel, the curve shows the best-fit model, while the shaded regions once again indicate the 68% and 95% ranges at each value of N_{200} . The breakdown of the total χ^2 by the different data sets is as follows: $\chi^2=6.1$, 6.5, and 5.7 for the $^{0.1}M_r < -19.5$, -20.5 , and -21.0 clustering samples, respectively. For the M/N data the $\chi^2=10.6$. Parameter values and uncertainties for the HOD parameters are given in Table 4, while cosmological constraints under various priors and assumptions are listed in Table 5. We note that the best-fit value of f_{sys} is 1.13—given our model assumptions, fitting the data favors M/N values 18% higher than our direct estimates, but within our estimated systematic uncertainty.

5.2. Cosmological Parameter Constraints

Figure 8 shows the main cosmological constraints in the Ω_m - σ_8 plane. In cluster abundance studies, there is a natural “banana curve” degeneracy between Ω_m and σ_8 ; the number of clusters above a fixed mass varies with the overall matter density, while the number of massive objects is highly sensitive to the amplitude of matter fluctuations. This degeneracy curve also exists for cluster M/L or M/N ratios, for the reasons described in §3.3. The shaded banana curve in Figure 8 shows the results of the Tinker et al. (2005) analysis. The degeneracy between Ω_m and σ_8 is still seen in our analysis, with a combined constraint of $\Omega_m^{0.5}\sigma_8 = 0.465 \pm 0.026$. The power on Ω_m was chosen such that the likelihood of the parameter combination was symmetric and yielded the smallest fractional error. Without adding any additional datasets

and marginalizing over all other parameters, the constraints on individual cosmological parameters are: $\Omega_m = 0.29 \pm 0.03$, $\sigma_8 = 0.85 \pm 0.06$ (68%). We emphasize that these constraints follow from SDSS galaxy clustering and maxBCG galaxy and weak lensing profiles, given only loose priors on the primordial power spectrum and the broad assumptions of our HOD framework. Combining these results with the latest constraints from WMAP7 (CMB-only constraints, assuming flat Λ CDM; Komatsu et al. 2010), our constraints are $\Omega_m = 0.280 \pm 0.012$, $\sigma_8 = 0.812 \pm 0.016$.

Although the Tinker et al. (2005) result overlaps with our 1σ error contour in the Ω_m - σ_8 plane, the best-fit value of the cluster normalization is higher in our current results. This offset is driven primarily by the differences in the amplitude of the M/N measurements from the maxBCG catalog relative to the mean M/L ratio of the 17 clusters in the CNOC2 survey. However, there are several marked differences in the present analysis. First, we model M/N as a function of cluster richness, as opposed to using the mean M/L ratio. Second, in Tinker et al. (2005) we fixed $\alpha_{\text{sat}} = 1$. In this paper, we find $1.0 \lesssim \alpha_{\text{sat}} \lesssim 1.1$ depending on luminosity. If we had fixed $\alpha_{\text{sat}} = 1.1$ in the previous analysis, this would yield a 6% increase in the $\Omega_m^{0.6}\sigma_8$ constraint (see Fig. 4 in Tinker et al. 2005). Lastly, systematic errors in the HOD modeling, as well as redshift evolution from the mean CNOC2 redshift $z \sim 0.3$, were not included in the Tinker et al. (2005) analysis. This would increase the errors and bring the two analyses into better statistical agreement.

Figure 9 illustrates the origin of the constraints in the Ω_m - σ_8 plan, using data from the $^{0.1}M_r < -20.5$ sample. We choose four models from the MCMC chain that lie on our 2σ contour, two that bracket the width of the $\Omega_m^{0.5}\sigma_8$ degeneracy axis (both σ_8 and Ω_m are low or high) and two that bracket the range of allowed models along a constant $\Omega_m^{0.5}\sigma_8$. Figure 9b plots that fractional discrepancies of each model with the $w_p(r_p)$ data, while Figure 9c compares the predicted and observed M/N . The M/N agreement appears acceptable in all cases, but that is because the M/N normalization systematic f_{sys} is allowed to vary. For the high and low $\Omega_m^{0.5}\sigma_8$ models, f_{sys} has been forced to unlikely values that account for much of the χ^2 . Figure 9d shows the M/N predictions when f_{sys} is fixed to our best-fit value of 1.13. In this case, the high and low $\Omega_m^{0.5}\sigma_8$ models predict M/N values that are clearly too high and too low, respectively. The two models that define the allowed range along the degeneracy axes are ruled out largely by their discrepancies with the clustering data, especially for the low- Ω_m , high- σ_8 model. Somewhat counter-intuitively, the discrepancies with $w_p(r_p)$ have the same sign in both cases, but the M/N data are also constraining the HOD—in the low- σ_8 model, lowering $\langle N_{\text{sat}} \rangle_M$ at high masses would reduce $w_p(r_p)$, but it would also raise M/N values are already too high.

Figure 10 demonstrates the effect of systematic uncertainties on our cosmological constraints. In the first panel, our uncertainties on the halo mass function, halo bias relation, and scale dependent bias, are reduced to 1%, 1% and 3%, respectively, which dramatically shrinks the allowed parameter range along the $\Omega_m^{0.5}\sigma_8$ degeneracy axis. The tightening of the constraints is due, in order of importance, to the reduced uncertainty in the large-scale bias, the scale-dependent bias, and the mass function. The uncertainty in the mass function has nearly negligible effect on the results, which demonstrates once again the distinction between M/N and cluster abundance constraints. The middle panel shows the effect of

the uncertainty on the systematics in the measurements—the evolution of the luminosity function, the HOD, and the weak lensing calibration, encapsulated by f_{sys} . Here we reduce the combined uncertainties to 1%, which leaves the range along the degeneracy curve unchanged but shrinks the width of the Ω_m - σ_8 degeneracy curve by about a factor of two. We note that once the prior on f_{sys} goes below 5%, the results are unchanged. At that level of precision, we are statistically limited by the M/N signal measured from the cluster sample. The far right panel shows the cosmological constraints when reducing both the theoretical and measurement uncertainties. For a given galaxy clustering measurement, the M/N data set the amplitude of the Ω_m - σ_8 degeneracy axis. The value of f_{sys} varies the amplitude of M/N , thus widening the error contours parallel to this axis. The shape and amplitude of the galaxy clustering measurements constrain the length of the error contours along the axis. By reducing the systematics, it would be possible to tighten the constraints on σ_8 and Ω_m to ~ 3 –5% from this technique alone, without any additional data sets (see the lower three rows in Table 5).

Figure 11 explores the effect of other priors in our analysis. In the left panel, we enforce a 10% Gaussian prior on the mass-concentration relation for satellite galaxies. This has minimal impact on the cosmological constraints, demonstrating the insensitivity of this approach to the details of the spatial bias of galaxies within clusters—our method is only sensitive to the mean number of satellites. The middle panel shows the effect on Ω_m - σ_8 if we tighten our priors on h_0 and n_s , which has the effect of narrowing the range of shapes of the linear matter power spectrum. Once again, there is little effect on cosmology from the shape of $P(k)$ —our method is most sensitive to its amplitude. The right panel assumes minimal error on the mass-richness relation and its scatter. Here again the change in the cosmological constraints is minimal.

Figure 12 shows the constraints on cosmological parameters as well as the marginalization parameters. In these contour plots one can see clearly the dependence of our cosmological parameters on f_{sys} , ϵ_b , and ϵ_r , as well as the lack of correlation with ϵ_n , h_0 , and n_s . Of our systematic uncertainties, ϵ_b (the normalization of the halo bias relation) shows the strongest degeneracies with the cosmological parameters Ω_m and σ_8 . The uncertainty on halo bias anticorrelates with σ_8 . The clustering data determines the parameter combination $b_{\text{gal}}\sigma_8$, thus the same fit to $w_p(r_p)$ can be achieved with a lower σ_8 and an artificially enhanced bias factor. Because the M/N data determine the $\Omega_m^{0.5}\sigma_8$ combination, ϵ_b shows a positive correlation with Ω_m to preserve the cluster normalization as σ_8 varies. The red curves plotted on top of the histograms represent the prior applied to that parameter. The histograms for h_0 , n_s , ϵ_b , and ϵ_n are coincident, or nearly so, with their priors. The best-fit marginalized values of ϵ_r and f_{sys} are $\sim -1.3\sigma$ and $+0.6\sigma$ off their prior values, respectively. For ϵ_r , a value below unity brings the scale-dependent bias formula closer to scale-independent. At scales below $\sim 1 h^{-1}$ Mpc, this increases the amplitude of the halo-halo clustering. The value of ϵ_r is positively correlated with σ_8 through their effect on $w_p(r_p)$ at the transition scale between pairs of galaxies in distinct halos and pairs of galaxies that exist within a single halo (commonly referred to as the ‘one-two to two-halo transition region’). Pairs of galaxies at the transition regime can come from both sources—satellite galaxies in massive halos and galaxy-galaxy pairs in smaller halos (that can be closer together). If two-halo clustering is higher at $r_p \lesssim 1 h^{-1}$ Mpc, there is less need for massive clusters to supply the pairs to fit

$w_p(r_p)$ at that scale. The offset between the MCMC results for f_{sys} and its prior indicate some tension between the clustering measurements and the maxBCG M/N data. Recall that f_{sys} multiplies the model calculations of M/N ; to fit the data with $f_{\text{sys}} = 1$ requires a higher σ_8 than is preferred by the clustering measurements. However this offset is within our uncertainty of the evolution between the redshifts of the two samples. Although circumstantial, it is worth noting that the best fit value of f_{sys} is consistent with the amount and direction of evolution in the HOD seen in the Bower et al. (2006) semi-analytic galaxy formation model (see Appendix B), and with the direction of the HOD evolution seen in our abundance matching models.

5.3. Halo Occupation Constraints

The 1σ parameter constraints for all three clustering samples are listed in Table 4. Figure 13 shows the constraints on the HOD parameters for the $^{0.1}M_r < -19.5$ clustering sample. There is a strong degeneracy between α_{sat} and M_{sat} . As M_{sat} increases, the number of galaxies in high mass halos decreases, but this can be compensated for by increasing α_{sat} . Tilting the $\langle N_{\text{sat}} \rangle_M$ power law has the effect of reducing the number of satellite galaxies in halos with $M < M_{\text{sat}}$. It is satellite galaxies in these low-mass halos that provide the pairs in the correlation function at the smallest scales probed by our $w_p(r_p)$ measurement, $r_p \lesssim 0.3 h^{-1}$ Mpc. Thus to fit $w_p(r_p)$, when α_{sat} and M_{sat} increase, M_{cut} decreases. In the best-fit model for this sample, satellite galaxies are more centrally concentrated than the dark matter by a factor of 1.6, but the constraints on this parameter are weak and not strongly correlated with any other HOD parameter.

For $^{0.1}M_r < -20.5$, shown in Figure 14, similar degeneracies are seen between α_{sat} , M_{sat} , and M_{cut} . There is a tail in the likelihood function for M_{cut} to low masses; when $M_{\text{cut}} \lesssim M_{\text{min}}$, M_{cut} no longer has an effect on the HOD or $w_p(r_p)$, thus all values below this mass scale are equally likely. Rather than place a prior on M_{cut} that depends on the value of M_{min} , we allow the chain to roam free through this part of parameter space, which yields unusual likelihood shapes. For this sample, values of $\sigma_{\log M} > 1$ are strongly excluded because larger values of the scatter decrease the large-scale bias of the sample and cannot be reconciled with the observations even given the range of σ_8 values probed in the MCMC chain. For this sample, the spatial distribution of the satellite galaxies is best represented by the concentration-mass relation adopted for the dark matter halos, but the constraints on f_{con} are also weak and do not depend on the other HOD parameters.

For the bright sample, shown in Figure 14, $\sigma_{\log M}$ is more tightly constrained; low values of the scatter produce too high a large-scale bias relative to the $w_p(r_p)$ measurements. A value of $\sigma_{\log M}$ that monotonically increases with galaxy luminosity is expected if the scatter in galaxy luminosity at fixed halo mass is a constant, as widely assumed. The strange likelihood function for M_{cut} is due to the fact that the $M_{\text{cut}} < M_{\text{min}}$ for most of the chain, as discussed above. The f_{con} parameter is unconstrained in this model; the error bars in the one-halo term are somewhat larger because of the smaller galaxy number density and the lower fraction of galaxies that are satellites relative to fainter samples (see, e.g., Z10).

For all three samples, the power-law index on the satellite occupation function, α_{sat} , is close to unity, as expected from theoretical studies and from previous analyses of SDSS clustering. There is some tension between our values of α_{sat} and those derived from the clustering-only analysis of Z10. For

TABLE 4
HOD PARAMETERS CONSTRAINTS

Name	$^{0.1}M_r < -19.5$	$^{0.1}M_r < -20.5$	$^{0.1}M_r < -21.5$
$\log M_{\min}$	11.59 ± 0.07	12.21 ± 0.11	12.87 ± 0.12
$\log M_{\text{sat}}$	12.94 ± 0.06	13.46 ± 0.05	13.87 ± 0.05
α_{sat}	1.01 ± 0.04	1.03 ± 0.05	1.08 ± 0.05
$\log M_{\text{cut}}$	$12.48^{+0.31}_{-0.24}$	$12.60^{+0.25}_{-0.29}$	$10.29^{+0.38}_{-0.89}$
$\log \sigma_{\log M}$	-0.69	$-0.54^{+0.40}_{-0.71}$	$-0.12^{+0.06}_{-0.08}$
f_{con}	$1.61^{+0.34}_{-0.44}$	$0.97^{+0.45}_{-0.23}$	$0.81^{+1.14}_{-0.55}$
f_{sat}	0.16 ± 0.02	0.15 ± 0.01	0.13 ± 0.01

NOTE. — All halo masses are in units of $h^{-1} \text{M}_{\odot}$. All logarithms are in base-10. f_{sat} is the fraction of galaxies that are satellites. We note that any comparison between these results and others should account for any difference in halo mass definition.

TABLE 5
COSMOLOGICAL PARAMETER CONSTRAINTS

Name	Ω_m	σ_8	$\Omega_m^{0.5} \sigma_8$
M/N	0.29 ± 0.03	0.85 ± 0.06	0.465 ± 0.026
$M/N + \text{counts}$	$0.280^{+0.020}_{-0.023}$	$0.809^{+0.044}_{-0.027}$	
$M/N + \text{WMAP7}$	0.290 ± 0.016	0.826 ± 0.020	
$M/N + \text{counts} + \text{WMAP7}$	0.280 ± 0.012	0.812 ± 0.016	
$M/N + \text{WMAP7} + \text{BAO} + H_0$	0.282 ± 0.011	0.819 ± 0.015	
			$\Omega_m^{0.5} \sigma_8$
M/N minus theory sys.	$0.276^{+0.026}_{-0.017}$	$0.908^{+0.045}_{-0.031}$	
M/N minus data sys.	$0.331^{+0.026}_{-0.036}$	$0.842^{+0.050}_{-0.041}$	$0.493^{+0.029}_{-0.010}$
M/N minus all sys.	$0.297^{+0.019}_{-0.012}$	$0.952^{+0.029}_{-0.030}$	

NOTE. — Results including “counts” refer to the results from Rozo et al. (2010). Results using WMAP7 data refer to seven-year CMB data from Komatsu et al. (2010). These results assume a flat Λ CDM cosmology. WMAP7 and WMAP7+BAO+ H_0 results are taken from the publicly available MCMC chains from <http://lambda.gsfc.nasa.gov/>. The bottom three parameter sets show constraints by reducing the errors on our systematics, as in Figure 10 (no additional data are included). ‘Minus theory’ means setting the priors on ϵ_n , ϵ_b , and ϵ_r to 1%, 1%, and 3%, respectively. ‘Minus data’ means setting the error on f_{sys} to 3%. ‘Minus all’ means combining both theory and data results.

$^{0.1}M_r < -20.5$, and $^{0.1}M_r < -21.0$, Z10 find $\alpha_{\text{sat}} = 1.15 \pm 0.03$ and $\alpha_{\text{sat}} = 1.15 \pm 0.06$, respectively. Our analysis yields $\alpha_{\text{sat}} = 1.03^{+0.04}_{-0.03}$ and $\alpha_{\text{sat}} = 1.08 \pm 0.05$. Some of this difference may be due to the choice of $\sigma_8 = 0.8$ in Z10; this is 1σ below our best-fit value. But to account for the full difference, the M/N data must be included. It is notable that our constraints on HOD parameters are not appreciably better than those of Z10 even with the addition of extra data on the HOD; however, Z10 fix their cosmology, which naturally tightens the constraints on the HOD parameters, and the include larger scale $w_p(r_p)$ data. Z10 use a cutoff power-law to parameterize $\langle N_{\text{sat}} \rangle_M$, as opposed to the exponential cutoff in eq. (7), and they assume $\Delta_{\text{halo}} = 200\rho_m$ for all calculations, thus a one-to-one comparison of the two is not straightforward.

6. DISCUSSION

6.1. Comparison to Cluster Abundance Studies

Throughout the analysis in this paper, the information from cluster number counts—i.e., the space density of clusters as a function of richness or mass—has not been used. Figure 16 compares our results to those of various cluster abundance studies. In particular, the left-hand side compares the cosmological constraints from M/N to those of abundances from maxBCG clusters (Roza et al. 2010). Both of these analy-

ses use the same sample of clusters, but in nearly complementary ways. The M/N results are both in good agreement with the abundance constraints and competitive with the abundance constraints. The right-hand side of Figure 16 presents the 95% confidence region in the Ω_m - σ_8 plane for the two maxBCG studies in comparison to several cluster abundance results from X-ray observations. Here again, the M/N results are in good agreement with and competitive with these approaches.

There are several ways in which the M/N approach is complementary to and independent of the cluster abundance method, even when using the same cluster sample. The parameters ϵ_r , ϵ_b , and the evolution of the luminosity function have no impact on abundance analysis. The dominant theoretical systematic uncertainty for cluster abundances is the shape and normalization of the halo mass function. From Figure 12, the dependence of cosmology on this uncertainty is nearly negligible. In the analysis of maxBCG counts by Roza et al. (2010), the dominant systematic uncertainties are miscentering and the normalization of the weak lensing mass calibration. Miscentering has less of an effect on M/N than on abundance analysis. The weak lensing measurements of Sheldon et al. (2009b) and halo mass estimates of Johnston et al. (2007) are used to calibrate the mass-richness

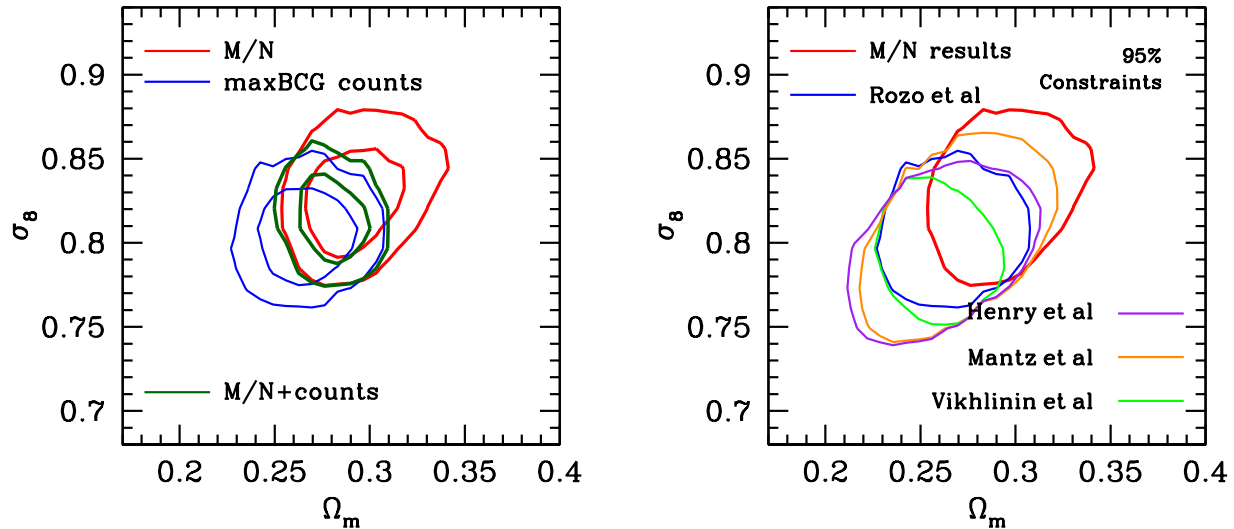


FIG. 16.— *Left Panel:* Comparison of the M/N results to parameter constraints from maxBCG cluster counts from Rozo et al. (2010). Both results assume WMAP7 priors. It is important to note that cluster abundances are not used anywhere in our analysis. The systematic uncertainties that Rozo et al. are most sensitive to are the ones on which M/N have little dependence. Thus, the constraints from these two studies are roughly independent. *Right Panel:* Comparison of this work to other cluster abundance studies. All contours are 95% and incorporate WMAP7 priors. The M/N technique is consistent and competitive with cluster abundance studies while using complementary information to cluster counts.

relation in the Rozo et al. (2010) results, thus the uncertainty in the weak-lensing calibration is correlated between the M/N and abundance analyses. However, this uncertainty is subdominant in the M/N analysis. Removal of this uncertainty entirely would only change the prior on f_{sys} from 0.227 to 0.225. A larger error in the weak lensing calibration than that suggested by Rozo et al. (2010) would affect both measurements. A fully robust analysis of the maxBCG cluster catalog should simultaneously model $N(N_{200})$, $w_p(r_p)$, and M/N , but given the different dependences of the techniques on the common systematic uncertainties, the two results can be considered nearly independent. Combined constraints using M/N , cluster counts, and CMB data are listed in Table 5. For non-optical cluster counts, such as detections through X-ray or Sunyaev-Zeldovich observations, the dominant observational systematics are the absolute normalization and scatter of the mass-observable relation. Because α_{sat} is close to unity for all galaxy samples, the M/N function is nearly independent of cluster richness and thus of scatter in mass versus richness. Figure 11 demonstrates the insensitivity of our results to our assumptions about the uncertainty in this scatter.

If the theoretical uncertainties on ϵ_n , ϵ_b , and ϵ_h were significantly smaller, our best fit value for σ_8 would be ~ 0.91 . This would be in tension with the WMAP7 cosmological constraints as well as cluster abundance results. This tension could be relieved if the true halo bias function had a higher normalization than the Tinker et al. (2010) result by $\sim 3\%$, or a scale-dependent bias that is closer to scale-independent relative to the non-linear dark matter clustering.

6.2. Prospects for the Future

Substantial improvements in the cosmological constraints presented in this paper can be achieved by reducing the systematic uncertainties in the current analysis. The theoretical uncertainties most applicable to our analysis, namely the large-scale bias and scale-dependent bias of dark matter halos, can be reduced with improved numerical simulations. Al-

though state-of-the-art just two years ago, the N-body simulation set analyzed in Tinker et al. (2008a) and Tinker et al. (2010) has been replicated many times over (in volume and particle number) by ongoing numerical studies. The simulations of the Las Damas project⁶ can currently achieve marked improvement in the halo mass function (McBride et al., in preparation) and the bias statistics for typical Λ CDM cosmologies. A fully robust theoretical framework requires understanding of halo populations in dark energy cosmologies, although we expect the impact of dark energy to be small at fixed Ω_m , σ_8 , and power spectrum shape (e.g., Kuhlen et al. 2005).

For the systematic uncertainties in our measurements, there exists a simple solution to remove the uncertainty on the evolution of the luminosity function and the HOD between the clustering samples and the sample of clusters: measure the clustering from the same volume of space as the maxBCG sample. A spectroscopic sample of luminous red galaxies (LRGs) with $\bar{n}_g \approx 1 \times 10^{-4}$ extends to $z = 0.36$ (see, e.g., Kazin et al. 2010). Nearly every maxBCG cluster above a richness limit of $N_{200} = 9$ ($M \approx 3 \times 10^{13} h^{-1} M_\odot$) should contain one or more LRGs (Zheng et al. 2009), thus this analysis can be repeated on a sample of LRGs with an uncertainty on f_{sys} than only comes from the weak lensing calibration. From the low number density of LRGs, as well as the halo occupation analysis of Zheng et al. (2009), we expect $\langle N_{\text{sat}} \rangle_M$ for LRGs to be roughly 1/4 that of the bright sample analyzed here, increasing the statistical errors on $\langle N_{\text{sat}} \rangle_M$ from $\sim 5\%$ to 10% , but the size of the maxBCG cluster sample analyzed can be increased by a factor of two relative to the sample used in Sheldon et al. (2009b) and in this paper. In the near future, the Baryon Oscillation Spectroscopic Survey (BOSS; Schlegel et al. 2009) will increase the number density of LRGs at $z \lesssim 0.4$ by a factor of three relative to the DR7 LRG number density. All of this points to luminous

⁶ <http://lss.phy.vanderbilt.edu/lasdamas/>

red galaxies as a logical and straightforward extension of the M/N analysis.

In the longer term, there are numerous photometric surveys planned that will produce vast numbers of optically-detected galaxy clusters out to $z \gtrsim 1$, including the Dark Energy Survey, Pan-STARRS, and the Large Synoptic Survey Telescope. These surveys are also designed for weak lensing in order to obtain cluster masses as well as cosmic shear to measure the amplitude of dark matter clustering. These surveys will yield precise measurements of the angular clustering of L_* galaxies. The M/N technique can be applied to these data with little modification from the analysis presented here. Due to the complementary nature of the M/N approach to cluster abundances, this technique will enhance the measurements on the growth and expansion history of the universe and tighten constraints on the equation of state of dark energy. For photometric data, the dominant systematic will be uncertainties in the photometric redshift errors, and it will be important to quantify how the effect of photometric redshift uncertainty correlates M/N and cluster abundance data. As opposed to cluster counts, which are sensitive both to the growth of structure and to the expansion history of the universe, the M/N approach is primarily sensitive to growth because the volume element does not enter directly into the M/N predictions. Thus the combination of these two approaches may break the degeneracy between dark energy and models in which gravity is modified at large scales in order to explain late-time acceleration (e.g., Knox et al. 2006; Huterer & Linder 2007).

7. SUMMARY

We have presented measurements of the mass-to-galaxy-number ratio (M/N) within maxBCG clusters in the SDSS. Combined with measurements of the projected clustering of galaxies, we have demonstrated that these data are a sensitive probe of the cosmological parameters Ω_m and σ_8 , while being insensitive to other cosmological parameters that mainly

enter into the shape of the linear matter power spectrum. Our theoretical analysis is based on the halo occupation distribution (HOD). We have incorporated uncertainties in the theoretical modeling, including uncertainties in the halo mass function, the halo bias function, and the scale-dependent bias of halos. We are most sensitive to uncertainties in the halo bias function and to the possibility of evolution between the mean redshift of the cluster sample, $z \sim 0.25$, and the mean redshift of the clustering sample, $z \sim 0.1$. After incorporating all these uncertainties in our analysis, we find $\Omega_m^{0.5} \sigma_8 = 0.465 \pm 0.026$, with individual constraints of $\Omega_m = 0.29 \pm 0.03$ and $\sigma_8 = 0.85 \pm 0.06$. Combined with current CMB data, these constraints are $\Omega_m = 0.290 \pm 0.016$ and $\sigma_8 = 0.826 \pm 0.020$. These constraints are consistent with and comparable to those obtained by cluster abundances, even though abundance information is not used in this analysis. Future investigations could reduce the systematic uncertainties in this analysis and thereby tighten parameter constraints by a factor of two or more.

The systematic uncertainties that are most important for cluster abundance studies, namely theoretical uncertainties in the halo mass function and scatter in the mass-observable relation, have negligible impact on the constraints achieved with M/N . Thus the combination of these two techniques can provide a unique probe of the growth and expansion history of the universe from future photometric galaxy surveys.

RHW received support from the DOE under contract DE-AC03-76SF00515. MTB and RHW thank their collaborators on the LasDamas project for critical input on the Carmen simulation, which was performed on the Orange cluster at SLAC. ER is funded by NASA through the Einstein Fellowship Program, grant PF9-00068. DHW acknowledges the support of NSF grant AST-1009505. IZ acknowledges support by NSF grant AST-0907947.

APPENDIX

A. MODIFIED SCALE-DEPENDENT BIAS

In this paper we use a modified form of the scale-dependent bias function presented in Tinker et al. (2005). That function was calibrated on a series of N-body simulations in which the halos were identified using the friends-of-friends percolation algorithm (FOF; e.g., Davis et al. 1985), with a linking length of 0.2 times the mean interparticle separation. The halo mass function and halo bias function used here use the spherical overdensity algorithm (SO; Tinker et al. 2008a, 2010). In FOF, nearby halos can be linked together and labeled as a single object. In SO, this rarely happens. In the SO algorithm implemented by Tinker et al., halos are allowed to overlap so long as the center of one halo is not within the virial radius of another. Thus the small-scale clustering of halos in these two scenarios should not be the same. For pair separations $r \geq R_1 + R_2$, the Tinker et al. (2005) function is an adequate description of the scale dependence of bias. For pairs in the overlap regime, $r < R_1 + R_2$, we find that the bias with respect to the non-linear matter distribution is nearly constant. Thus we adopt

$$b^2(M, r) = \begin{cases} b^2(M) \frac{[1+1.17 \xi_m(r)]^{1.49}}{[1+0.69 \xi_m(r)]^{2.09}} & \text{if } r \geq 2R_{\text{halo}} \\ b^2(M) \frac{[1+1.17 \xi_m(2R_{\text{halo}})]^{1.49}}{[1+0.69 \xi_m(2R_{\text{halo}})]^{2.09}} & \text{if } r < 2R_{\text{halo}} \end{cases} \quad (\text{A1})$$

as our functional form. At $r < R_{\text{halo}}$, $b(M, r) = 0$ by definition, but this is enforced in the halo exclusion of the two-halo term. See Appendix B of Tinker et al. (2005) for full details on the analytic model, with the minor differences described in §3.1.

Figure C17 shows the halo autocorrelation functions for five mass bins. The data points are taken from two simulations described in Tinker et al. (2010): L1000W and H384. Results are shown here for halos with $N \geq 400$ particles per halo. The curves are calculated assuming $\xi(r) = b^2(M, r) \xi_m(r)$, where $\xi_m(r)$ is the non-linear matter correlation function given by Smith et al. (2003). The dotted curves show the original function and the solid curves show the modification in eq. (A1). It is clear that eq. (A1) is a better description of halo-halo clustering at small scales. The fit is not perfect, however, which is why we have adopted a 15% error on the deviation of the bias from scale independence.

B. EVOLUTION OF THE HOD IN SEMI-ANALYTIC MODELS

One of our primary uncertainties is whether the HOD measured at $z = 0.25$ should be the same as that inferred from clustering at $z = 0.1$. In a separate paper we will demonstrate that the halo occupation of galaxies inferred through the subhalo abundance matching paradigm shows negligible evolution for samples defined at a fixed number density (Reddick et al., in preparation). We have also investigated the evolution of the HOD in the semi-analytic galaxy formation model of Bower et al. (2006), built upon the high resolution Millennium N-body simulation (Springel et al. 2005). This model compares well with the observed luminosity and color distribution of galaxies, and it does a reasonable job reproducing the dependence of galaxy properties on environment (Baldry et al. 2006). Figure C18 shows the evolution of the HOD for galaxies in the SA model for the same three number density thresholds as our $z = 0.1$ clustering samples. In each panel, the upper frame shows the HOD at $z = 0.25$, $z = 0.1$ and $z = 0$. The lower frame shows the ratio of $\langle N \rangle_{Mz=0.25}$ to $\langle N \rangle_M$ at $z = 0.1$ and $z = 0$. For the halo mass range probed by the maxBCG sample, and over the redshift baseline of our observations, $\langle N \rangle_M$ varies by 5-10%, depending on the galaxy number density. We incorporate a 10% uncertainty in the evolution of the HOD in our analysis.

C. TESTS WITH MOCK GALAXIES

We have tested our methodology on mock galaxy distributions created on a high-resolution N-body simulation. The simulation is H384 from the simulation set analyzed in Tinker et al. (2008a, 2010). The simulation consists of 1024^3 particles evolved in a volume $384 h^{-1}$ Mpc per side. The mass resolution of this simulation is high enough to resolve halos well below M_{\min} of the $0.1 M_r < -19.5$ galaxy sample. The simulation cosmology is $(\Omega_m, \sigma_8, \Omega_b, h_0, n_s) = (0.3, 0.90, 0.04, 0.7, 1.0)$. The halo catalogs are the same as those in the Tinker et al. mass function and bias relation analyses, using the SO halo finder.

Our procedure for creating the mock data was as follows. First, we fit the $w_p(r_p)$ data alone assuming the same cosmology as the simulation. The halos within the simulation are populated with galaxies according to the best-fit HODs. For each halo, a maxBCG richness N_{200} is assigned according to the mass-richness relation given in eq. (10) (including scatter). The halos are stacked in the same richness bins given in Table 2, and the mean value of M/N for each bin is calculated directly from the set of halos in each bin; i.e., we do not create shear profiles or projected number density profiles from the galaxy distribution. Our test was directed at the methodology of combining $w_p(r_p)$ and M/N itself, rather than the techniques for measuring these quantities, which are tested elsewhere and are included in the systematic error budget in our analysis. We include all the same systematic uncertainties in this analysis—halo statistics, mass-richness relation, cosmological parameters—except for f_{sys} , which we fixed at unity and do not allow to vary. We obtain the error bars on $w_p(r_p)$ from performing the jackknife technique on the simulation itself, but for M/N we adopt the same (proportional) errors as on the maxBCG data.

Figure C19 shows the cosmological constraints produced by the mock analysis. The error contours are centered on the input cosmology. The banana curve is similar to the results from the actual data but with a stronger constraint on the cluster normalization due to the tight prior on f_{sys} .

REFERENCES

- Abazajian, K. N. et al. 2009, *ApJS*, 182, 543
 Abbas, U. et al. 2010, *MNRAS*, 406, 1306
 Adelman-McCarthy, J. K. et al. 2006, *ApJS*, 162, 38
 Bahcall, N. A., Cen, R., Davé, R., Ostriker, J. P., & Yu, Q. 2000, *ApJ*, 541, 1
 Bahcall, N. A., Lubin, L. M., & Dorman, V. 1995, *ApJ*, 447, L81+
 Baldry, I. K., Balogh, M. L., Bower, R. G., Glazebrook, K., Nichol, R. C., Bamford, S. P., & Budavari, T. 2006, *MNRAS*, 373, 469
 Bardeen, J. M., Bond, J. R., Kaiser, N., & Szalay, A. S. 1986, *ApJ*, 304, 15
 Becker, M. R., McKay, T. A., Koester, B., Wechsler, R. H., Rozo, E., Evrard, A., Johnston, D., Sheldon, E., Annis, J., Lau, E., Nichol, R., & Miller, C. 2007, *ApJ*, 669, 905
 Behroozi, P. S., Conroy, C., & Wechsler, R. H. 2010, *ApJ*, 717, 379
 Berlind, A. A. & Weinberg, D. H. 2002, *ApJ*, 575, 587
 Berlind, A. A., Weinberg, D. H., Benson, A. J., Baugh, C. M., Cole, S., Davé, R., Frenk, C. S., Jenkins, A., Katz, N., & Lacey, C. G. 2003, *ApJ*, 593, 1
 Blanton, M. R. 2006, *ApJ*, 648, 268
 Blanton, M. R., Hogg, D. W., Bahcall, N. A., Brinkmann, J., Britton, M., Connolly, A. J., Csabai, I., Fukugita, M., Loveday, J., Meiksin, A., Munn, J. A., Nichol, R. C., Okamura, S., Quinn, T., Schneider, D. P., Shimasaku, K., Strauss, M. A., Tegmark, M., Vogeley, M. S., & Weinberg, D. H. 2003, *ApJ*, 592, 819
 Blanton, M. R. & Roweis, S. 2007, *AJ*, 133, 734
 Bower, R. G., Benson, A. J., Malbon, R., Helly, J. C., Frenk, C. S., Baugh, C. M., Cole, S., & Lacey, C. G. 2006, *MNRAS*, 370, 645
 Boylan-Kolchin, M., Springel, V., White, S. D. M., & Jenkins, A. 2010, *MNRAS*, 406, 896
 Bullock, J. S., Kolatt, T. S., Sigad, Y., Somerville, R. S., Kravtsov, A. V., Klypin, A. A., Primack, J. R., & Dekel, A. 2001, *MNRAS*, 321, 559
 Busha, M. T., Wechsler, R. H., Behroozi, P. S., Gerke, B. F., Klypin, A. A., & Primack, J. R. 2010, *ApJ*, submitted (arXiv:1011.6373)
 Carlberg, R. G., Yee, H. K. C., Ellingson, E., Abraham, R., Gravel, P., Morris, S., & Pritchet, C. J. 1996, *ApJ*, 462, 32
 Cole, S. & Kaiser, N. 1989, *MNRAS*, 237, 1127
 Conroy, C., Wechsler, R. H., & Kravtsov, A. V. 2006, *ApJ*, 647, 201
 Cooray, A. & Sheth, R. 2002, *Phys. Rep.*, 372, 1
 Croton, D. J., Gao, L., & White, S. D. M. 2007, *MNRAS*, 374, 1303
 Davis, M., Efstathiou, G., Frenk, C. S., & White, S. D. M. 1985, *ApJ*, 292, 371
 Eisenstein, D. J. & Hu, W. 1999, *ApJ*, 511, 5
 Gao, L., Frenk, C. S., Boylan-Kolchin, M., Jenkins, A., Springel, V., & White, S. D. M. 2011, *MNRAS*, 410, 2309
 Gao, L. & White, S. D. M. 2006
 Gerdes, D. W., Sypniewski, A. J., McKay, T. A., Hao, J., Weis, M. R., Wechsler, R. H., & Busha, M. T. 2010, *ApJ*, 715, 823
 Gott, III, J. R., Schramm, D. N., Tinsley, B. M., & Gunn, J. E. 1974, *ApJ*, 194, 543
 Hansen, S. M., McKay, T. A., Wechsler, R. H., Annis, J., Sheldon, E. S., & Kimball, A. 2005, *ApJ*, 633, 122
 Hansen, S. M., Sheldon, E. S., Wechsler, R. H., & Koester, B. P. 2009, *ApJ*, 699, 1333
 Hu, W. & Kravtsov, A. V. 2003, *ApJ*, 584, 702
 Huterer, D. & Linder, E. V. 2007, *Phys. Rev. D*, 75, 023519
 Jenkins, A., Frenk, C. S., White, S. D. M., Colberg, J. M., Cole, S., Evrard, A. E., Couchman, H. M. P., & Yoshida, N. 2001, *MNRAS*, 321, 372
 Johnston, D. E., Sheldon, E. S., Wechsler, R. H., Rozo, E., Koester, B. P., Frieman, J. A., McKay, T. A., Evrard, A. E., Becker, M. R., & Annis, J. 2007, *ApJ*, submitted (arXiv:0709.1159)
 Kazin, E. A., Blanton, M. R., Scoccimarro, R., McBride, C. K., Berlind, A. A., Bahcall, N. A., Brinkmann, J., Czarapata, P., Frieman, J. A., Kent, S. M., Schneider, D. P., & Szalay, A. S. 2010, *ApJ*, 710, 1444
 Klypin, A., Trujillo-Gomez, S., & Primack, J. 2010, *ApJ*, submitted (arXiv:1001.3660)
 Knox, L., Song, Y., & Tyson, J. A. 2006, *Phys. Rev. D*, 74, 023512
 Koester, B. P., McKay, T. A., Annis, J., Wechsler, R. H., Evrard, A., Bleem, L., Becker, M., Johnston, D., Sheldon, E., Nichol, R., Miller, C., Scranton, R., Bahcall, N., Barentine, J., Brewington, H., Brinkmann, J., Harvanek, M., Kleinman, S., Krzesinski, J., Long, D., Nitta, A., Schneider, D. P., Snedden, S., Voges, W., & York, D. 2007a, *ApJ*, 660, 239
 Koester, B. P., McKay, T. A., Annis, J., Wechsler, R. H., Evrard, A. E., Rozo, E., Bleem, L., Sheldon, E. S., & Johnston, D. 2007b, *ApJ*, 660, 221
 Komatsu, E., Smith, K. M., Dunkley, J., Bennett, C. L., Gold, B., Hinshaw, G., Jarosik, N., Larson, D., Nolta, M. R., Page, L., Spergel, D. N., Halpern, M., Hill, R. S., Kogut, A., Limon, M., Meyer, S. S., Odegard, N., Tucker, G. S., Weiland, J. L., Wollack, E., & Wright, E. L. 2010, *ApJ*, submitted (arXiv:1001.4538)
 Kravtsov, A. V., Berlind, A. A., Wechsler, R. H., Klypin, A. A., Gottlöber, S., Allgood, B., & Primack, J. R. 2004, *ApJ*, 609, 35
 Kuhlen, M., Strigari, L. E., Zentner, A. R., Bullock, J. S., & Primack, J. R. 2005, *MNRAS*, 357, 387

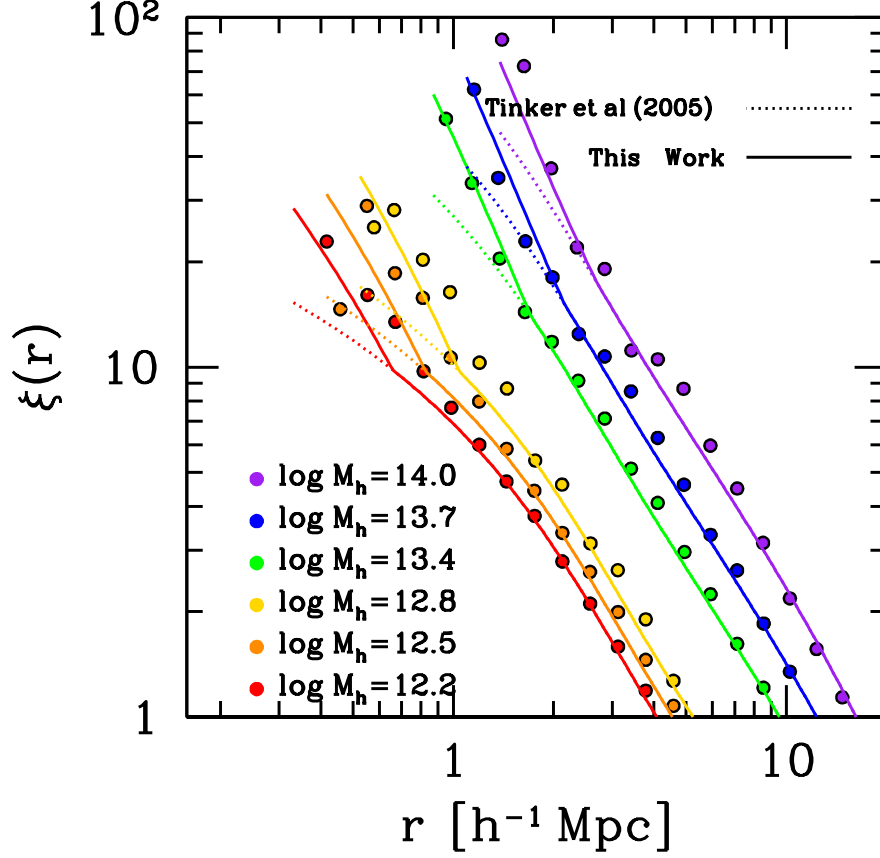


FIG. C17.— Halo-halo correlation functions from two high resolution N-body simulations (the L1000W and H384 simulations utilized to calibrate both the halo mass function and halo bias relation in Tinker et al. 2008a and Tinker et al. 2010). The three low-mass bins are from the H384 simulation and the three high-mass bins are from the L1000W simulation. The abrupt increase in clustering amplitude between the two simulation results is due to the change in cosmological model. The dotted line shows the scale-dependent bias function of Tinker et al. (2005). The solid curves show our modification to this formula to account for the change in halo definition between the Tinker et al. (2005) simulations and the more recent calibrations. See text for details.

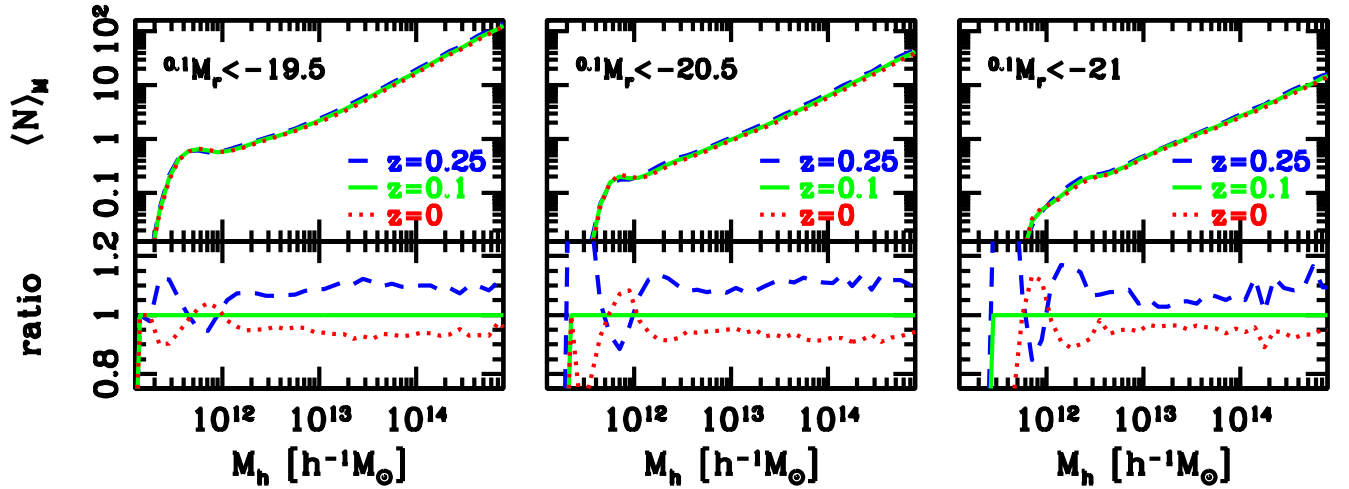


FIG. C18.— Evolution of the HOD in the Bower et al. (2006) semi-analytic galaxy formation model. The right, middle, and left panels show results for galaxy samples that match the number densities of our $0.1 M_r < -21$, $0.1 M_r < -20.5$, and $0.1 M_r < -19.5$ samples, respectively. The lower frame in each panel shows the ratio with respect to the $z = 0.1$ HOD.

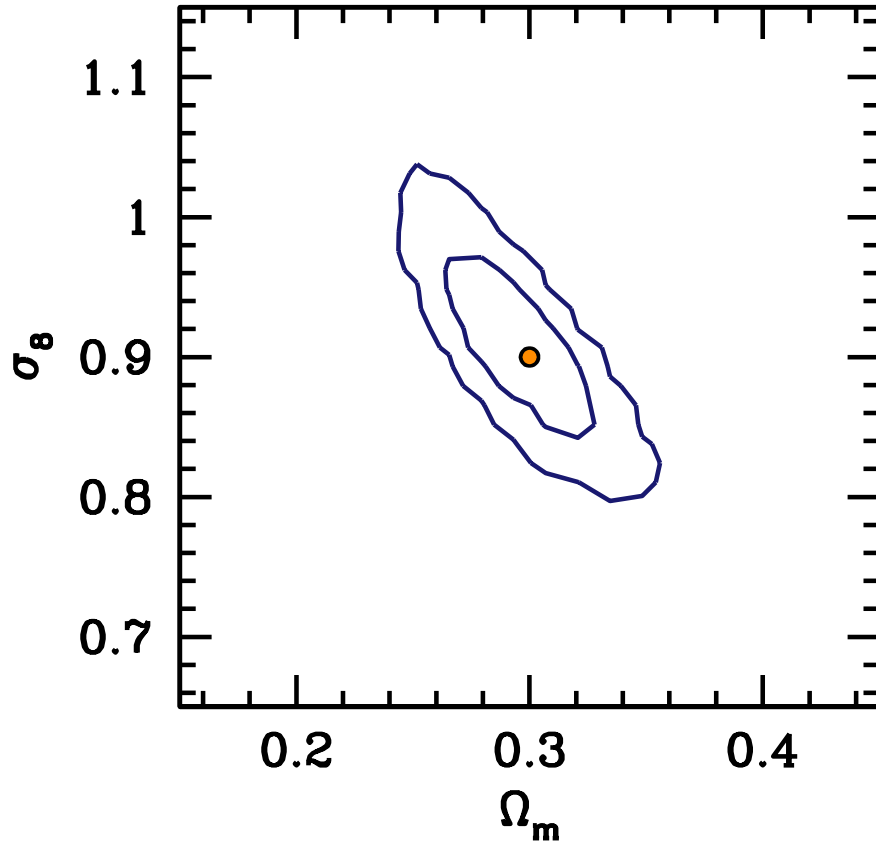


FIG. C19.— Cosmological constraints on mock data created from an N-body simulation $384\ h^{-1}\text{Mpc}$ per side (the H384 simulation utilized to calibrate both the halo mass function and halo bias relation in Tinker et al. 2008a and Tinker et al. 2010). The mock analysis incorporates uncertainties on ϵ_n , ϵ_r , and ϵ_b , but assume that $f_{\text{sys}} = 1$ with no error. The circle indicates the input cosmology.

- Lin, Y.-T., Mohr, J. J., & Stanford, S. A. 2004, *ApJ*, 610, 745
- Ma, C., Maggiore, M., Riotto, A., & Zhang, J. 2010, *MNRAS*, submitted (arXiv:1007.4201)
- Mo, H. J. & White, S. D. M. 1996, *MNRAS*, 282, 347
- Moster, B. P., Somerville, R. S., Maulbetsch, C., van den Bosch, F. C., Macciò, A. V., Naab, T., & Oser, L. 2010, *ApJ*, 710, 903
- Navarro, J. F., Frenk, C. S., & White, S. D. M. 1997, *ApJ*, 490, 493
- Norberg, P., Baugh, C. M., Gaztañaga, E., & Croton, D. J. 2009, *MNRAS*, 396, 19
- Norberg, P., Baugh, C. M., Hawkins, E., Maddox, S., Peacock, J. A., Cole, S., Frenk, C. S., Bland-Hawthorn, J., Bridges, T., Cannon, R., Colless, M., Collins, C., Couch, W., Dalton, G., De Propris, R., Driver, S. P., Efstathiou, G., Ellis, R. S., Glazebrook, K., Jackson, C., Lahav, O., Lewis, I., Lumsden, S., Madgwick, D., Peterson, B. A., Sutherland, W., & Taylor, K. 2001, *MNRAS*, 328, 64
- Peacock, J. A. & Smith, R. E. 2000, *MNRAS*, 318, 1144
- Peebles, P. J. E. 1986, *Nature*, 321, 27
- Pillepich, A., Porciani, C., & Hahn, O. 2010, *MNRAS*, 402, 191
- Press, W. H. & Schechter, P. 1974, *ApJ*, 187, 425
- Reed, D. S., Bower, R., Frenk, C. S., Jenkins, A., & Theuns, T. 2007, *MNRAS*, 374, 2
- Rines, K., Geller, M. J., Diaferio, A., Kurtz, M. J., & Jarrett, T. H. 2004, *AJ*, 128, 1078
- Rozo, E., Rykoff, E. S., Evrard, A., Becker, M., McKay, T., Wechsler, R. H., Koester, B. P., Hao, J., Hansen, S., Sheldon, E., Johnston, D., Annis, J., & Frieman, J. 2009, *ApJ*, 699, 768
- Rozo, E., Wechsler, R. H., Rykoff, E. S., Annis, J. T., Becker, M. R., Evrard, A. E., Frieman, J. A., Hansen, S. M., Hao, J., Johnston, D. E., Koester, B. P., McKay, T. A., Sheldon, E. S., & Weinberg, D. H. 2010, *ApJ*, 708, 645
- Rykoff, E. S., McKay, T. A., Becker, M. R., Evrard, A., Johnston, D. E., Koester, B. P., Rozo, E., Sheldon, E. S., & Wechsler, R. H. 2008, *ApJ*, 675, 1106
- Schlegel, D., White, M., & Eisenstein, D. 2009, in *White Paper Submitted to The Astronomy and Astrophysics 2010 Decadal Survey* (arXiv:0902.4680)
- Scoccimarro, R., Sheth, R. K., Hui, L., & Jain, B. 2001, *ApJ*, 546, 20
- Seljak, U. 2000, *MNRAS*, 318, 203
- Seljak, U., Makarov, A., McDonald, P., Anderson, S. F., Bahcall, N. A., Brinkmann, J., Burles, S., Cen, R., Doi, M., Gunn, J. E., Ivezić, Ž., Kent, S., Loveday, J., Lupton, R. H., Munn, J. A., Nichol, R. C., Ostriker, J. P., Schlegel, D. J., Schneider, D. P., Tegmark, M., Berk, D. E., Weinberg, D. H., & York, D. G. 2005, *Phys. Rev. D*, 71, 103515
- Seljak, U. & Warren, M. S. 2004, *MNRAS*, 355, 129
- Sheldon, E. S., Johnston, D. E., Masjedi, M., McKay, T. A., Blanton, M. R., Scranton, R., Wechsler, R. H., Koester, B. P., Hansen, S. M., Frieman, J. A., & Annis, J. 2009a, *ApJ*, 703, 2232
- Sheldon, E. S., Johnston, D. E., Scranton, R., Koester, B. P., McKay, T. A., Oyaizu, H., Cunha, C., Lima, M., Lin, H., Frieman, J. A., Wechsler, R. H., Annis, J., Mandelbaum, R., Bahcall, N. A., & Fukugita, M. 2009b, *ApJ*, 703, 2217
- Sheth, R. K., Mo, H. J., & Tormen, G. 2001, *MNRAS*, 323, 1
- Sheth, R. K. & Tormen, G. 1999, *MNRAS*, 308, 119
- Simha, V., Weinberg, D., Dave, R., Fardal, M., Katz, N., & Oppenheimer, B. D. 2010, *MNRAS*, (submitted) arXiv:1011.4964
- Smith, R. E., Peacock, J. A., Jenkins, A., White, S. D. M., Frenk, C. S., Pearce, F. R., Thomas, P. A., Efstathiou, G., & Couchman, H. M. P. 2003, *MNRAS*, 341, 1311
- Spergel, D. N., Bean, R., Doré, O., Nolte, M. R., Bennett, C. L., Dunkley, J., Hinshaw, G., Jarosik, N., Komatsu, E., Page, L., Peiris, H. V., Verde, L., Halpern, M., Hill, R. S., Kogut, A., Limon, M., Meyer, S. S., Odgaard, N., Tucker, G. S., Weiland, J. L., Wollack, E., & Wright, E. L. 2007, *ApJS*, 170, 377
- Spergel, D. N., Verde, L., Peiris, H. V., Komatsu, E., Nolte, M. R., Bennett, C. L., Halpern, M., Hinshaw, G., Jarosik, N., Kogut, A., Limon, M., Meyer, S. S., Page, L., Tucker, G. S., Weiland, J. L., Wollack, E., & Wright, E. L. 2003, *ApJS*, 148, 175
- Springel, V., White, S. D. M., Jenkins, A., Frenk, C. S., Yoshida, N., Gao, L., Navarro, J., Thacker, R., Croton, D., Helly, J., Peacock, J. A., Cole, S., Thomas, P., Couchman, H., Evrard, A., Colberg, J., & Pearce, F. 2005, *Nature*, 435, 629
- Tegmark, M., Strauss, M. A., Blanton, M. R., Abazajian, K., Dodelson, S., Sandvik, H., Wang, X., Weinberg, D. H., Zehavi, I., Bahcall, N. A., Hoyle, F., Schlegel, D., Scoccimarro, R., Vogeley, M. S., Berlind, A., Budavari, T., Connolly, A., Eisenstein, D. J., Finkbeiner, D., Frieman, J. A., Gunn, J. E., Hui, L., Jain, B., Johnston, D., Kent, S., Lin, H., Nakajima, R., Nichol, R. C., Ostriker, J. P., Pope, A., Scranton, R., Seljak, U., Sheth, R. K., Stebbins, A., Szalay, A. S., Szapudi, I., Xu, Y., Annis, J., Brinkmann, J., Burles, S., Castander, F. J., Csabai, I., Loveday, J., Doi, M., Fukugita, M., Gillespie, B., Hennessy, G., Hogg, D. W., Ivezić, Ž., Knapp, G. R., Lamb, D. Q., Lee, B. C., Lupton, R. H., McKay, T. A., Kunszt, P., Munn, J. A., O'Connell, L., Peoples, J., Pier, J. R., Richmond, M., Rockosi, C., Schneider, D. P., Stoughton, C., Tucker, D. L., vanden Berk, D. E., Yanny, B., & York, D. G. 2004, *Phys. Rev. D*, 69, 103501
- Tinker, J., Kravtsov, A. V., Klypin, A., Abazajian, K., Warren, M., Yepes, G., Gottlöber, S., & Holz, D. E. 2008a, *ApJ*, 688, 709
- Tinker, J. L. 2007, *MNRAS*, 374, 477
- Tinker, J. L., Conroy, C., Norberg, P., Patiri, S. G., Weinberg, D. H., & Warren, M. S. 2008b, *ApJ*, 686, 53
- Tinker, J. L., Norberg, P., Weinberg, D. H., & Warren, M. S. 2007, *ApJ*, 659, 877
- Tinker, J. L., Robertson, B. E., Kravtsov, A. V., Klypin, A., Warren, M. S., Yepes, G., & Gottlöber, S. 2010, *ApJ*, submitted, ArXiv:1001.3162
- Tinker, J. L., Weinberg, D. H., Zheng, Z., & Zehavi, I. 2005, *ApJ*, 631, 41
- Vale, A. & Ostriker, J. P. 2006, *MNRAS*, 371, 1173
- van den Bosch, F. C., Mo, H. J., & Yang, X. 2003, *MNRAS*, 345, 923
- van den Bosch, F. C., Yang, X., Mo, H. J., Weinmann, S. M., Macciò, A. V., More, S., Cacciato, M., Skibba, R., & Kang, X. 2007, *MNRAS*, 376, 841
- Warren, M. S., Abazajian, K., Holz, D. E., & Teodoro, L. 2006, *ApJ*, 646, 881
- Wechsler, R. H. 2004, *Clusters of Galaxies: Probes of Cosmological Structure and Galaxy Evolution*
- Wechsler, R. H., Zentner, A. R., Bullock, J. S., Kravtsov, A. V., & Allgood, B. 2006, *ApJ*, 652, 71
- Wetzel, A. R. & White, M. 2010, *MNRAS*, 403, 1072
- Yang, X., Mo, H. J., Jing, Y. P., van den Bosch, F. C., & Chu, Y. 2004, *MNRAS*, 350, 1153
- Yang, X., Mo, H. J., & van den Bosch, F. C. 2008, *ApJ*, 676, 248
- Yoo, J., Tinker, J. L., Weinberg, D. H., Zheng, Z., Katz, N., & Davé, R. 2006, *ApJ*, 652, 26
- York, D. G. et al. 2000, *AJ*, 120, 1579
- Zehavi, I., Zheng, Z., Weinberg, D. H., Blanton, M. R., Bahcall, N. A., Berlind, A. A., Brinkmann, J., Frieman, J. A., Gunn, J. E., Lupton, R. H., Nichol, R. C., Percival, W. J., Schneider, D. P., Skibba, R. A., Strauss, M. A., Tegmark, M., & York, D. G. 2010, *ApJ*, submitted (arXiv:1005.2413)
- Zehavi, I., Zheng, Z., Weinberg, D. H., Frieman, J. A., Berlind, A. A., Blanton, M. R., Scoccimarro, R., Sheth, R. K., Strauss, M. A., Kayo, I., Suto, Y., Fukugita, M., Nakamura, O., Bahcall, N. A., Brinkmann, J., Gunn, J. E., Hennessy, G. S., Ivezić, Ž., Knapp, G. R., Loveday, J., Meiksin, A., Schlegel, D. J., Schneider, D. P., Szapudi, I., Tegmark, M., Vogeley, M. S., & York, D. G. 2005, *ApJ*, 630, 1
- Zheng, Z., Berlind, A. A., Weinberg, D. H., Benson, A. J., Baugh, C. M., Cole, S., Davé, R., Frenk, C. S., Katz, N., & Lacey, C. G. 2005, *ApJ*, 633, 791
- Zheng, Z., Coil, A. L., & Zehavi, I. 2007, *ApJ*, 667, 760
- Zheng, Z., Tinker, J. L., Weinberg, D. H., & Berlind, A. A. 2002, *ApJ*, 575, 617
- Zheng, Z. & Weinberg, D. H. 2007, *ApJ*, 659, 1
- Zheng, Z., Zehavi, I., Eisenstein, D. J., Weinberg, D. H., & Jing, Y. P. 2009, *ApJ*, 707, 554
- Zhu, G., Zheng, Z., Lin, W. P., Jing, Y. P., Kang, X., & Gao, L. 2006, *ApJ*, 639, L5